DEUTSCHES ELEKTRONEN-SYNCHROTRON
Ein Forschungszentrum der Helmholtz-Gemeinschaft

DESY-THESIS-2018-014
May 2018

A Simulation Framework for Studying High Intensity X-Ray Induced Dynamics and Scattering Patterns from Nanocrystals

by

M. M. Abdullah

ISSN 1435-8085

NOTKESTRASSE 85 - 22607 HAMBURG

DESY behält sich alle Rechte für den Fall der Schutzrechtserteilung und für die wirtschaftliche Verwertung der in diesem Bericht enthaltenen Informationen vor.

DESY reserves all rights for commercial use of information included in this report, especially in case of filing application for or grant of patents.

To be sure that your reports and preprints are promptly included in the
HEP literature database
send them to (if possible by air mail):

DESY	DESY
Zentralbibliothek Notkestraße 85 22607 Hamburg Germany	Bibliothek Platanenallee 6 15738 Zeuthen Germany

A simulation framework for studying high intensity x-ray induced dynamics and scattering patterns from nanocrystals

Dissertation zur Erlangung des Doktorgrades
des Fachbereiches Physik
der Universität Hamburg

vorgelegt von

Malik Muhammad Abdullah

Hamburg

2017

Gutachter der Dissertation: Prof. Dr. Robin Santra
Prof. Dr. Henry N. Chapman

Gutachter der Disputation: Prof. Dr. Robin Santra
Prof. Dr. Beata Ziaja-Motyka
Dr. Adrian Mancuso
Dr. Anton Barty

Datum der Disputation: November 6th, 2017.

Vorsitzender des Fach-Promotionsausscuhsses: Prof. Dr. Daniela Pfannkuche

Leiter des Fachbereiches Physik: Prof. Dr. Michael Potthoff

Dekan der Fakultät für Mathematik,
Informatik und Naturwissenschaften: Prof. Dr. Heinrich Graener

Declaration of Authorship

I herewith declare, on oath, that I have produced this thesis without the prohibited assistance of third parties and without making use of aids other than those specified. This thesis has not been presented previously in identical or similar form to any other German or foreign examination board. Moreover, the publications included in the thesis are properly cited and were published for the completion of this thesis.

Hiermit erkläre ich an Eides statt, dass ich die vorliegende Dissertationsschrift selbst verfasst und keine anderen als die angegebenen Quellen und Hilfsmittel benutzt habe.

Hamburg, den Unterschrift

Abstract

A standard method of reconstructing the structure of a protein in its crystalline phase is by x-ray diffraction. New generation x-ray sources, the X-ray free-electron lasers (XFEL), provide novel opportunities for biomolecular structure determination. The extreme intensity and ultrashort pulse duration of an XFEL pulse make it feasible to extend the diffraction technique towards nano sized crystals. However, during a high-intensity measurement, significant atomic and electronic dynamics occur that affect the diffraction signal. Simulations of the ionization dynamics of an irradiated nanocrystal and the diffraction pattern formed are computationally expensive. To overcome this bottleneck, I have developed a methodology implemented as computer codes. I have applied the methodology for specific problems: for identifying the characteristic features of the spatial beam profile imprinted on the scattering pattern, analyzing effective form factors at high intensity and in studies of high energy density plasma formation.

Deutsche version: Eine Standardmethode für die Rekonstruktion der Proteinstruktur in seiner kristallinen Phase ist die Röntgenbeugung. Eine neue Generation von Röntgenstrahlungsquellen, wie der Freie-Elektronen-Laser für Röntgenstrahlung (XFEL), bietet neue Möglichkeiten für die biomolekulare Strukturbestimmung. Die extreme Intensität und die ultrakurze Pulsdauer eines XFEL-Pulses ermöglicht es, die Beugungstechnik auf Nanokristalle zu erweitern. Jedoch treten bei diesen Hochintensitätsmessungen signifikante atomare und elektronische Dynamiken auf, die das Beugungssignal beeinflussen. Die Simulation der Ionisationsdynamik eines bestrahlten Nanokristalls und das gebildete Beugungsmuster sind rechnerisch kostenintensiv. Um diesen Nachteil zu überwinden, habe ich eine Methodik entwickelt in Form speziell implementierter Computercodes. Diese Methodik

habe ich auf spezifische Probleme angewandt: Zur Identifizierung von charakteristischen Merkmalen des räumlichen Strahlprofils geprägt durch das Streuungsmuster, die Analyse effektiver Formfaktoren bei hoher Intensität und in Studien zur Plasmabildung bei hohen Energiedichten.

Acknowledgements

With a deep sense of gratitude, I would like to thank Prof. Robin Santra for his valuable guidance and time towards the project. I admire the way he is so involved with all the projects and still has the capacity to take out time on a regular basis for us. I appreciate the discussions that I asked for on a very short notice and they went on for hours and hours. Besides being better in research, I have learnt to be spontaneous from him (and, yes, one more thing, which is actually a quote – "You cannot compare apples and oranges"). I would like to thank Prof. Beata Ziaja Motyka for guiding me throughout my Ph.D. time and keeping me on my toes.

I had an amazing time in the group and for that, I would like to thank, firstly, Zoltan Jurek. I have learnt a lot from Zoltan and had, most probably, the longest discussions. Besides being a good colleague, he is a great friend indeed. I would also like to thank Sang-Kil Son for the amazing discussions that we had. He never even once got tired of the discussions that we had and always have motivated me to bring the best out of me. I would like to mention Otfried Geffert (THE ROOT). He has always given me the best advices so for that I am really thankful to him. It will not be good if I don't mention my buddies Murali Krishna and John Bekx. I will not thank them for the good time because they don't actually care about thanks, they just need food and good stuff (Gustav). I would like to specially thanks Helma and Manfred for being so caring. They never made me think even for once that I am away from my home. I would like to thanks Nikita Medvedev, Sophia Bazzi, Yi-Jen Chen, Antonia Karamatskou, Caroline Arnold and Daria Kolbasova for the amazing time that I had in Ph.D. time duration. I would like to thanks all my family specially my sisters Amna Malik and Zulaikha Malik. I would like to thank Gourab for the best times that we had together in Europe. Words are inadequate to express the gratitude that I have for Gourab. At the end, I would like to thank two most

important women in my life my nani ami (grand mother) and my mother (Mariam Malik). I would specially like to thank my mother for making me what I am today. Without her, I would have been nothing. I love you the most mama.

Contents

Abstract **v**

Acknowledgements **vii**

List of publications **xxiii**

1 Introduction **1**

2 Theoretical framework **7**

2.1 XATOM 7

2.1.1 Theoretical and numerical procedure 8

2.1.2 X-ray absorption cross-section 10

2.1.3 Auger decay 11

2.1.4 Fluorescence 12

2.1.5 Coherent x-ray scattering 12

2.1.6 Average-atom model 13

2.2 XMDYN 16

2.2.1 Overview 16

2.2.2 Molecular Dynamics 16

2.2.3 XMDYN code structure 17

2.2.4 Monte Carlo block 18

2.2.5 Impact ionization and recombination 19

2.2.6 Electron plasma analysis 20

2.3 Extensions of XMDYN 20

2.3.1 Periodic boundary conditions (PBC) using minimum image convention 21

2.3.2 PBC using Ewald summation 22

2.3.3 Construction of a nanocrystal 29

3 Radiation damage in solid-density matter 31

3.1 A molecular-dynamics approach for studying thermalization properties of x-ray-heated solid-density matter 31

3.1.1 Motivation 31

3.1.2 Molecular dynamics with super-cell approach 32

3.2 Validation of the methodology 33

3.3 Application 40

4 XSINC: X-ray scattering in nanocrystals 45

4.1 Calculation of x-ray scattering patterns from nanocrystals at high x-ray intensity 46

4.1.1 Motivation 46

4.1.2 Methodology of simulating scattering pattern 46

4.1.3 Super-cell approach for scattering signal evaluation 47

4.1.4 Results and Discussion 50

4.2 Towards the theoretical limitations of x-ray nanocrystallography at high intensity: the validity of the effective-form-factor description . . 58

4.2.1 Motivation 58

4.3 Theoretical methods 59

4.4 Numerical analysis 61

4.4.1 Simulation methods 61

4.4.2 Results 62

5 Application: imaging of progressing radiation damage in real time 69

5.1 Setup: sample and simulation conditions 70

5.1.1 Results and Discussion on radiation damage 71

5.1.2 Results and Discussion on scattering intensity and patterns . 75

6 Conclusions 81

A Effective-form-factors derivation 85

References 95

List of Figures

2.1 Diagrams of x-ray-induced processes calculated by XATOM. P: photoionization; A: Auger decay; F: fluorescence; SO: shake-off; S: Rayleigh and Compton x-ray scattering; RS: resonant elastic x-ray scattering. This figure is taken from Ref. [1] 8

2.2 Flowchart of XMDYN, showing the separation and the sequence of different blocks. It also shows on the fly connection with XATOM to calculate various atomic parameters. This figure is taken from Ref. [1]. 18

3.1 Time evolution of the temperature of the electron plasma within XMDYN simulation during and after x-ray irradiation at different fluences: (a) $\mathcal{F}_{\text{low}} = 6.7\times10^{9}\,\text{ph}/\mu\text{m}^2$, (b) $\mathcal{F}_{\text{med}} = 1.9\times10^{11}\,\text{ph}/\mu\text{m}^2$ and (c) $\mathcal{F}_{\text{high}} = 3.8\times10^{11}\,\text{ph}/\mu\text{m}^2$. In all three cases, the pulse duration is 10 fs FWHM; the pulse is centered at 20 fs, and the photon energy is 1 keV. The black curve represents the gaussian temporal envelope. Note that in all cases, equilibrium is reached within 100 fs after the pulse. This figure is taken from Ref. [2]. 34

3.2 Relation between plasma temperature and energy absorbed per atom in AA calculations for a carbon system of mass density $0.07\text{g}/\text{cm}^3$. This figure is taken from Ref. [2]. 35

3.3 Kinetic-energy distribution of the electron plasma and charge-state distributions from AA and XMDYN simulations (250 fs after the irradiation) for low fluence (a,b), medium fluence (c,d), and high fluence (e,f). This figure is taken from Ref. [2]. 38

3.4 Average energy absorbed per atom within diamond irradiated with a Gaussian pulse of hard and soft x rays of ω_{ph} = 5000 eV, $I_{\text{max}} = 10^{18}\,\text{W/cm}^2$ and ω_{ph} = 1000 eV, $I_{\text{max}} = 10^{16}\,\text{W/cm}^2$, respectively. In both cases, a pulse duration of 10 fs FWHM was used. This figure is taken from Ref. [2]. 39

3.5 Average charge within diamond irradiated with a Gaussian pulse of hard and soft x rays of (a) ω_{ph} = 5000 eV, $I_{\text{max}} = 10^{18}\,\text{W/cm}^2$ and (b) ω_{ph} = 1000 eV, $I_{\text{max}} = 10^{16}\,\text{W/cm}^2$, respectively. In both cases, a pulse duration of 10 fs FWHM was used. This figure is taken from Ref. [2]. 39

3.6 Comparison of impact ionization cross sections for neutral ground-state carbon atom used in the current work within XMDYN based on the BEB formula [3], and the cross sections used in the continuum approach of Ref. [4] based on experimental data. This figure is taken from Ref. [2]. 41

3.7 Average atomic charge in I3C as a function of time for (a) $\mathcal{F}_{\text{med}} = 5.0\times10^{12}\,\text{ph}/\mu\text{m}^2$ and (b) $\mathcal{F}_{\text{high}} = 1.0\times10^{13}\,\text{ph}/\mu\text{m}^2$, respectively. In both cases, a pulse duration of 10 fs FWHM was used. The photon energy was 9.7 keV. This figure is taken from Ref. [2]. 43

3.8 Kinetic-energy distribution of the electron plasma in I3C from XMDYN simulations (250 fs after the irradiation) for the medium fluence (a) and the high fluence (b). This figure is taken from Ref. [2]. 43

4.1 Convergence of time integrated peak intensity for the reflection (1 1 1) as a function of the number of realizations per fluence point: (a) for the gaussian and (b) for the flattop spatial pulse profile. For the gaussian case, 350 different fluence points are used to calculate the time integrated intensity. This figure is taken from Ref. [5] 51

4.2 Radial fluence distributions in the current study: gaussian profile (spatially non-uniform case) and flattop profile (uniform within the irradiated part of the crystal). The focal size is 100 nm in both cases and the pulse energy is also considered to be same. This figure is taken from Ref. [5]. 52

4.3 Ionization dynamics of carbon atoms at different fluences: time dependent charge state populations of isolated carbon atoms calculated with XATOM for (a) $\mathcal{F}_{\text{high}} = 1 \times 10^{14}\,\mu\text{m}^{-2}$ and (b) $\mathcal{F}_{\text{mid}} = 4.5 \times 10^{13}\,\mu\text{m}^{-2}$. Similarly, time dependent charge state populations of carbon atoms in diamond calculated with XMDYN for (c) $\mathcal{F}_{\text{high}}$ and (d) $\mathcal{F}_{\text{mid}}$. Secondary ionization events enhance the overall ionization in a dense environment. The x-ray pulse with 10 fs FWHM temporal profile is centered at $t = 0$ fs. This figure is taken from Ref. [5]. 53

4.4 Mean displacement of the atoms for fluences $\mathcal{F}_{\text{high}} = 1\times10^{14}\,\mu m^{-2}$ (red dots), $\mathcal{F}_{\text{mid}} = 4.5\times10^{13}\,\mu m^{-2}$ (blue dots) and $\mathcal{F}_{\text{low}} = 6.0\times10^{12}\,\mu m^{-2}$ (green dots). The gaussian temporal pulse envelope is also depicted with the dashed black line. $\mathcal{F}_{\text{high}}$ is the fluence for the flattop profile, which is also the maximum fluence in the present study. $\mathcal{F}_{\text{mid}}$ and $\mathcal{F}_{\text{low}}$ are two values representing intermediate and low fluences taken from the gaussian profile case. The mean atomic displacement remains below the achievable resolution (~ 1.2Å) at 10keV for all the cases. This figure is taken from Ref. [5]. 55

4.5 Snapshots of the scattering intensity for reflection (1 1 1) along the $Q_y = Q_z = 1\,\text{Å}^{-1}$ line in reciprocal space: (a) gaussian spatial beam profile, (b) flattop spatial beam profile. Solid and dashed lines with the same color correspond to the same instantaneous irradiating x-ray intensities. Note that the negative and the corresponding positive times are of equal intensity during the rise and fall of the pulse envelope. (c,d) Total time integrated scattering signal for gaussian and flattop spatial beam profiles, respectively. Note the different vertical axis scales. This figure is taken from Ref. [5]. 57

4.6 Contour plot for the Bragg spot of reflection (1 1 1) in the $Q_z = 1\,\text{Å}^{-1}$ plane in reciprocal space: (a) Gaussian beam profile; (b) flattop beam profile. This figure is taken from Ref. [5]. 57

4.7 Real-space snapshots of ionization dynamics of a supercell comprising 105 molecules of glycine. The photon energy is 10 keV; the peak intensities are $I_3 = 1.5 \times 10^{20}\,\text{W/cm}^2$ and $I_4 = 1.5 \times 10^{21}\,\text{W/cm}^2$. The temporal pulse envelope is Gaussian with 10 fs full width at half maximum (FWHM). This figure is taken from Ref. [6] 63

4.8 Average charge as a function of time at the intensity of (a) $I_1 = 1.5 \times 10^{18}\,\mathrm{W/cm^2}$, (b) $I_2 = 1.5 \times 10^{19}\,\mathrm{W/cm^2}$, (c) $I_3 = 1.5 \times 10^{20}\,\mathrm{W/cm^2}$ and (d) $I_4 = 1.5 \times 10^{21}\,\mathrm{W/cm^2}$. The red curve represents the temporal Gaussian envelope of 10 fs FWHM. This figure is taken from Ref. [6] 64

4.9 Crystallographic R-factor in two different cases as a function of intensity. The black bars represent $R_{\mathrm{eff,re}}$, the brown bars represent $R_{\bar{\mathrm{f}}_{\mathrm{X}},\mathrm{re}}$. This figure is taken from Ref. [6] 65

4.10 Relative differences of the effective form factor (f_X^{eff}) as compared to the ideal form factor (f_X^0) for different atomic species. The peak intensity for each panel is the same as used in Fig. 4.8. This figure is taken from Ref. [6] 66

5.1 Average charge as a function of time, representing (a) 0 fs delay, where the two pulses are coincident, (b) 20 fs delay, (c) 40 fs delay, (d) 80 fs delay and (e) 110 fs delay. The black curve represents the temporal Gaussian envelope of 10 fs FWHM. The fluence considered is $\mathcal{F}_{\mathrm{med}} = 5.0\times10^{12}\,\mathrm{ph}/\mu\mathrm{m}^2$; the average charge is calculated using 50 trajectories for each delay. 71

5.2 Average charge as a function of time, representing (a) 0 fs delay, where the two pulses are coincident, (b) 20 fs delay, (c) 40 fs delay, (d) 80 fs delay and (e) 110 fs delay. The black curve represents the temporal Gaussian envelope of 10 fs FWHM. The fluence considered is $\mathcal{F}_{\mathrm{high}} = 1.0\times10^{13}\,\mathrm{ph}/\mu\mathrm{m}^2$; the average charge is calculated using 50 trajectories for each delay. 72

5.3 Mean displacement as a function of time, representing (a) 0 fs delay, where the two pulses are coincident, (b) 20 fs delay, (c) 40 fs delay (d) 80 fs delay and (e) 110 fs delay. The black curve represents the temporal Gaussian envelope of 10 fs FWHM. The fluence considered is $\mathcal{F}_{\mathrm{med}} = 5.0{\times}10^{12}\,\mathrm{ph}/\mu\mathrm{m}^2$; the mean displacement is calculated using 50 trajectories for each delay. 73

5.4 Mean displacement as a function of time, representing (a) 0 fs delay, where the two pulses are concident, (b) 20 fs delay, (c) 40 fs delay, (d) 80 fs delay and (e) 110 fs delay. The black curve represents the temporal Gaussian envelope of 10 fs FWHM. The fluence considered is $\mathcal{F}_{\mathrm{high}} = 1.0{\times}10^{13}\,\mathrm{ph}/\mu\mathrm{m}^2$; the mean displacement is calculated using 50 trajectories for each delay case. 74

5.5 Time and volume integrated scattering intensity as a function of time delay, corresponding to Bragg reflections (a) (1 1 1), (b) (2 2 2), (c) (3 3 3), (d) (4 4 4), (e) (5 5 5) and (f) (6 6 6). The red curve represents the scattering intensity without the contribution of the free electrons, whereas the blue curve represents the scattering intensity from both bound and free electrons. The fluence considered is $\mathcal{F}_{\mathrm{med}} = 5.0{\times}10^{12}\,\mathrm{ph}/\mu\mathrm{m}^2$. 75

5.6 Time and volume integrated scattering intensity as a function of time delay, corresponding to Bragg reflections (a) (1 1 1), (b) (2 2 2), (c) (3 3 3), (d) (4 4 4), (e) (5 5 5) and (f) (6 6 6). The red curve represents the scattering intensity without the contribution of the free electrons, whereas the blue curve represents the scattering intensity from both bound and free electrons. The fluence considered is $\mathcal{F}_{\mathrm{high}} = 1.0{\times}10^{13}\,\mathrm{ph}/\mu\mathrm{m}^2$. 76

5.7 Contour plot for the Bragg reflection (1 1 1) in the $\mathrm{Q_z} = 1\,\mathrm{\mathring{A}}^{-1}$ plane in reciprocal space for $\mathcal{F}_{\mathrm{med}} = 5.0\times10^{12}\,\mathrm{ph}/\mu\mathrm{m}^2$. Figures (a-e) correspond to the scattering intensity including the free-electron term, whereas Figs. (f-j) illustrate the scattering intensity without the free-electron term. 78

5.8 Contour plot for the Bragg reflection (3 3 3) in the $\mathrm{Q_z} = 1\,\mathrm{\mathring{A}}^{-1}$ plane in reciprocal space for $\mathcal{F}_{\mathrm{med}} = 5.0\times10^{12}\,\mathrm{ph}/\mu\mathrm{m}^2$. Figures (a-e) correspond to the scattering intensity including the free-electron term, whereas Figs. (f-j) illustrate the scattering intensity without the free-electron term. 78

5.9 Contour plot for the Bragg reflection (1 1 1) in the $\mathrm{Q_z} = 1\,\mathrm{\mathring{A}}^{-1}$ plane in reciprocal space for $\mathcal{F}_{\mathrm{med}} = 1.0\times10^{13}\,\mathrm{ph}/\mu\mathrm{m}^2$. Figures (a-e) correspond to the scattering intensity including the free-electron term, whereas Figs. (f-j) illustrate the scattering intensity without the free-electron term. 79

5.10 Contour plot for the Bragg reflection (3 3 3) in the $\mathrm{Q_z} = 1\,\mathrm{\mathring{A}}^{-1}$ plane in reciprocal space for $\mathcal{F}_{\mathrm{med}} = 1.0\times10^{13}\,\mathrm{ph}/\mu\mathrm{m}^2$. Figures (a-e) correspond to the scattering intensity including the free-electron term, whereas Figs. (f-j) illustrate the scattering intensity without the free-electron term. 79

List of Tables

2.1 CPU timings for 1000 particles 29
2.2 GPU timings for 1000 particles 29

3.1 Final temperatures obtained from XMDYN runs after 250 fs propagation and from AA calculations. XMDYN temperatures are obtained from fitting using Eq. (2.32), while AA temperatures are obtained from the absorbed energy–temperature relation (Fig. 3.2). This table is taken from Ref. [2]. 36

4.1 Convergence parameters for calculating scattering intensity with XS-INC and their values in the current study. This table is taken from Ref. [5] 51

List of Publications

1. ***"Spatial beam profile-induced effects in x-ray scattering pattern at high intensity",***
   M. M. Abdullah, Z. Jurek, S.-K. Son, R. Santra, *J. Phys. Conf. Ser.* **635**, 102008 (2015).

2. ***"Calculation of x-ray scattering patterns from nanocrystals at high x-ray intensity",***
   M. M. Abdullah, Z. Jurek, S.-K. Son, R. Santra, *Struct. Dyn.* **3**, 054101 (2016).

3. ***"A molecular-dynamics approach for studying the non-equilibrium behavior of x-ray-heated solid-density matter",***
   M. M. Abdullah, Anurag, Z. Jurek, S.-K. Son, R. Santra, *Phys. Rev. E*, **96**, 023205 (2017).

4. ***"Towards the theoretical limitations of x-ray nanocrystallography at high intensity: the validity of the effective-form-factor description",***
   M. M. Abdullah, S.-K. Son, Z. Jurek, R. Santra, **Manuscript submitted** (2018).

This thesis is dedicated to Atif Shahbaz and Kiran Mahmmod. Thank you for being there for me…

Chapter 1

Introduction

Unraveling the structural changes in photo-triggered biomolecules has evoked great interest for decades [7, 8, 9, 10]. Recent advances in X-ray free electron laser (XFEL) sources [11, 12] have opened new horizons in the field of time-resolved x-ray crystallography. XFELs provide intense radiation of wavelengths comparable to atomic scales. They deliver intense femtosecond pulses that promise to yield high-resolution diffraction data of nanocrystals ($\sim$200 nm to 2 μm in size) before the destruction of the nanocrystal by radiation damage [13, 14]. The characteristics of XFEL radiation and associated sample environments have triggered the development of new data collection methods such as serial femtosecond crystallography (SFX) [15]. SFX is also an important step towards the ultimate goal and dream – to perform atomic-resolution single-particle imaging [16, 17, 18, 19, 20, 21].

Sample damage by x-rays and low signal-to-noise ratio at high photon momentum transfer limit the resolution of structural studies on non-repetitive structures such as individual biomolecules or cells. Therefore, at high resolution, SFX is currently still a better option to use. In SFX, a complete data-set can be obtained by exposing thousands of randomly oriented, individual nanocrystals of proteins to the x-ray beam.

Imaging nanocrystals of proteins and viruses at atomic resolution calls for high-intensity and short-duration x-ray pulses [22, 23, 16, 24, 25, 26]. The shortcoming of using high intensities is the rapid ionization of the atoms on a few-femtosecond timescale, which affects the structure of the protein. This radiation-induced damage changes the atomic form factors [27, 28] and may induce significant atomic displacement on longer timescales, which leads to the annihilation of the Bragg spots.

In an XFEL experiment, the biomolecular nanocrystals are injected in a jet and the individual XFEL pulses typically irradiate single nanocrystals at a time in random orientations, while the scattering pattern is recorded. In principle, using phase-retrieval algorithms [29, 30, 31, 32], the electron density may be determined and the positions of the atomic species predicted, although this often poses a serious challenge. The scattered electromagnetic field is directly related to the electron density through a mathematical operation (Fourier transform). However, in an imaging experiment, information about the phases of the scattered field is lost. In order to overcome this so-called “phase problem”, various techniques are in use. One example is that of isomorphous replacement, in which few of the atoms are replaced by heavy atomic species so that they can perturb the scattering pattern. Consequently, one can estimate the positions of the heavy atomic species and can thereby obtain possible values for the phase angle. Another similar technique is that of multi-wavelength anomalous diffraction or dispersion [33, 34, 35, 36, 37, 38] (MAD), which uses embedded atomic species known as anomalous scatterers. By using x-rays of different wavelengths around the absorption edge of the species, one can change the degree of perturbation of the scattering pattern due to the anomalous scatterers. In order to improve the scattering signal due to the diffraction, nanocrystals and highly symmetric molecules are often used [16, 20, 39, 40, 18].

For a comprehensive theoretical study of signal formation in an SFX experiment, one needs to simulate the radiation-induced dynamics of the sample and pattern-formation based on the dynamics. During the past decade, several models have been developed for studying the time evolution of small and large samples irradiated by XFEL pulses [41, 42, 31, 43, 44, 45, 46, 47, 48]. The bottleneck one faces is that it is computationally not feasible to simulate a nanocrystal (other systems can be simulated) with realistic size using tools that are capable of following the dynamics of each atom, required for imaging studies.

In order to give a complete description of the evolution of the atomic states in a sample, one needs to account for the possible occurrence of all electronic configurations of the atoms/ions. A computationally demanding situation arises when a sample consists of heavy atomic species [49, 50]. For example, at a photon energy of 5.5 keV, the number of electronic configurations accessible in a heavy atom such as xenon (Z=54) is about 20 million [50]. If one wants to describe the accessible configuration space of two such atoms, one must deal with $(2 \times 10^7)^2 = 4 \times 10^{14}$ electronic configurations. It is clear that following the population of all electronic configurations in a polyatomic sample as a function of time is a formidable task. To avoid this problem, the approximation of using superconfigurations has long been used [51, 52, 53]. Moreover, the approach of using a set of average configurations [54, 55] and the approach of limiting the available configurations by using a pre-selected subset of configurations in predominant relaxation paths [4] has been applied.

In $Chapter$ 2, I will discuss the theoretical framework used to simulate the effect of ultrafast XFEL pulses incident on a nanocrystal. To follow the time-evolution of the nanocrystal, I have developed an extension of XMDYN [1, 56, 57], which is a complex simulation tool for modeling dynamics of molecular systems (e.g. biological molecules) irradiated by an intense hard x-ray pulse. Using the original XMDYN code, simulation of a large number of particles in a nanocrystal is too expensive. I present a model, employing our extension of XMDYN, that is capable of describing this challenging situation. Moreover, in the last section of *Chapter* 2, I will briefly explain the theoretical formalism to calculate rates and cross-sections for different atomic processes using the XATOM toolkit. I will also explain an approach based on concepts of average-atom models [58] used in plasma physics [59, 60, 61, 62, 63].

Chapter 3 is based on a publication [2]. It includes the results and discussions based on the theoretical formalism defined in *Chapter* 2. I simulate the effect of individual ultrafast XFEL pulses of different intensities incident on a model system of carbon atoms placed on a lattice and analyze the quasi-equilibrium plasma state of the material reached through ionization and electron-plasma thermalization. To this end, I use two different tools. One is XMDYN with a periodic boundary condition extension and the other is the XATOM average-atom model (AA). I compare the electron temperatures and ion charge-state distributions provided by XMDYN and AA. I also make a comparison between predictions for the ionization dynamics in an irradiated diamond nanocrystal, obtained by the XMDYN particle approach, and results from a Boltzmann continuum approach published recently [4]. With these comparisons, I demonstrate the potential of the XMDYN code for the description of high-energy-density bulk systems in and out of equilibrium. Moreover, I consider a complex system of 5-amino-2,4,6-triiodoisophthalic acid (I3C in crystalline form), consisting of heavy and light atomic species. I demonstrate that XMDYN can simulate the dynamics of x-ray-driven complex matter with all the possible electronic configurations without pre-selecting any pathways in the electronic configuration space.

Chapter 4 is comprised of a publication based on a code XSINC [64, 5] – a tool based on a generalized method to describe the x-ray scattering intensity of the

Bragg reflections in a diffraction pattern from nanocrystals exposed to intense x-ray pulses. I present an approach that involves the division of a nanocrystal into smaller units (super-cells) and the calculation of their dynamics individually using periodic boundary conditions (PBC). In order to investigate the effect of inhomogeneous spatial fluence distribution, the super-cells are subjected to different fluences. Subsequently, I combine all the super-cells to form a nano-crystal and construct the scattering pattern under the influence of uniform (within the irradiated part of the sample) and non-uniform spatial beam profiles. I study and compare these two scenarios. The last section of this chapter is based on publication Ref. [6]. I will redefine the effective-form-factors, emphasizing their implications for the interpretation of the scattering patterns. A time-integrated pattern does not correspond to a static electron density via Fourier transform in a mathematically rigorous manner. It is formed by an incoherent sum of non-identical, individually coherent patterns. Therefore, it is not straightforward that conventional pattern-processing schemes can be expected to work. However, if the temporal-variance-aided effective-form-factor description is proven to be accurate under relevant damage conditions, it also ensures that the time-integrated pattern can be treated as a coherent pattern to good accuracy and image processing algorithms can be expected to converge and deliver a solution. By using a realistic radiation damage model including both atomic and environmental effects, I theoretically investigate the limitations of the simple effective-form-factor concept on the example of a glycine ($\mathrm{C_2H_5NO_2}$) organic nanocrystal. By calculating Bragg intensities we analyze the contribution of the temporal variance and the threshold pulse intensity up to which the constructed effective form factors are valid to describe the non-ideal patterns, thus allowing for the use of conventional crystallography processing methods.

$Chapter$ 5 is based on an experiment that was performed at the Linac Coherent

Light Source (LCLS), a hard X-ray FEL in USA. I will demonstrate the start-to-end simulations for calculating scattering patterns from a nanocrystal exposed to intense XFEL pulses.

$Chapter\ 6$ comprises the conclusions of the work presented in this thesis.

Chapter 2

Theoretical framework

In this chapter, I present the theoretical background to understand the radiation damage in bulk systems. The first section proceeds towards our in-house tool XATOM, an *ab-initio* x-ray atomic physics toolkit. In the second section, I will explain in detail XMDYN, our in-house Monte-Carlo (MC)-molecular dynamics (MD) code. In order to proceed within the framework of this thesis, the next section includes the extensions of XMDYN for the spatial periodic boundary conditions.

2.1 XATOM

XATOM [28, 65] is a toolkit for X-ray atomic physics. It gives a theoretical description of the fundamental processes in X-ray-atom interactions. It calculates atomic data-orbitals and the orbital energies, cross sections and rates for x-ray-induced processes like photoionization, x-ray fluorescence, Auger decay, elastic x-ray scattering along with its dispersion correction [35], Compton scattering [66] and shake-off branching ratios [67].

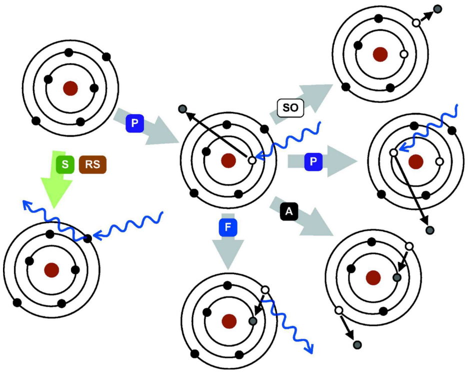

FIGURE 2.1: Diagrams of x-ray-induced processes calculated by XATOM. P: photoionization; A: Auger decay; F: fluorescence; SO: shake-off; S: Rayleigh and Compton x-ray scattering; RS: resonant elastic x-ray scattering. This figure is taken from Ref. [1]

.

2.1.1 Theoretical and numerical procedure

In order to implement the *ab-initio* framework [68], the Hartree-Fock-Slater (HFS) [69, 70] model is used. Local density approximation to the exact exchange interaction is employed. In this approximation, the many-particle Schrödinger equation is reduced to an effective single-electron Schrödinger equation:

$$\left[-\frac{1}{2}\nabla^2 + V(\mathbf{r})\right]\psi(\mathbf{r}) = \varepsilon\psi(\mathbf{r}), \tag{2.1}$$

where $\psi(\mathbf{r})$ represents an atomic orbital and ε is the corresponding orbital energy. The potential is given by

$$V(\mathbf{r}) = -\frac{Z}{r} + \int \frac{\rho(\mathbf{r}')}{|\mathbf{r}-\mathbf{r}'|}\, d^3r' - \frac{3}{2}\left[\frac{3}{\pi}\rho(\mathbf{r})\right]^{1/3}, \tag{2.2}$$

where Z is the nuclear charge of the atom, $\rho(\mathbf{r})$ represents the electron density, which is assumed to be spherically symmetric, and the spin polarization is averaged. The last term in the above equation is the exchange term, which is approximated by the

Slater exchange potential [69]. In addition, for numerical convergence reasons, the potential includes the Latter tail correction [71]. The electronic density $\rho(\mathbf{r})$ is given by

$$\rho(\mathbf{r}) = \sum_{i}^{N_{elec}} \psi_i^{\dagger}(\mathbf{r})\psi_i(\mathbf{r}), \tag{2.3}$$

where i is the spin-orbital index and N_{elec} is the number of electrons. The problem becomes spherically symmetric once angular momentum averaging is done. Each solution of Eq. (2.1) can be expressed in terms of the product of a radial wave function and a spherical harmonic. As an example, a bound-state spatial orbital with quantum numbers (n, l, m) may be written as

$$\psi_{nlm}(\mathbf{r}) = \frac{P_{nl}(r)}{r} Y_l^m(\theta, \phi). \tag{2.4}$$

The radial wavefunction $P_{nl}(r)$ is solved by the generalized pseudospectral method [72, 73] for bound states using a non-uniform grid. For continuum states, $P_{\varepsilon}(r)$ is numerically solved by the fourth-order Runge-Kutta method for a given energy ε on a uniform grid [74, 75]. To evaluate integrals involving both bound and continuum states, spline interpolation is used to map the bound-state orbitals from the non-uniform grid to the denser uniform grid, employed for the continuum states. For the bound state calculations, the theoretical procedure here is similar to Herman-Skillman code [76]. The numerical part of the present toolkit utilizes a different grid method, as it has the following advantages:

1. It is easy to control convergence with respect to the grid parameters.
2. One can avoid truncation of the maximum radius internally imposed by the Herman-Skillman code.

3. The matrix eigenvalue problem is solved by a modern linear algebra package [77].

XATOM toolkit is capable of calculating cross sections and rates for any possible electronic configuration. For example, a neutral carbon atom has $1s^2 2s^2 2p^2$ ground state configuration. The total number of possible electronic configurations for carbon is 27. XATOM performs a separate HFS calculation for each configuration. In other words, the orbitals are optimized in the presence of core and/or valence vacancies. Thus, orbital relaxation for the core-hole configurations is automatically included, a strategy which is known to be in good agreement with multiconfigurational self-consistent-field calculations [78].

2.1.2 X-ray absorption cross-section

The cross-section for ionizing an electron in the ith subshell by absorbing an x-ray photon with energy ω is given by [68]

$$\sigma_{\mathrm{P}}(i,\omega) = \frac{4}{3}\alpha\,\pi^2\,\omega N_i \sum_{l_j=|l_i-1|}^{l_i+1} \frac{l_>}{2\,l_i+1}\left|\int_0^\infty P_{n_i l_i}(r) P_{\varepsilon\, l_j}(r) r dr\right|^2, \tag{2.5}$$

where α is the fine-structure constant, N_i represents the occupation number of the ith subshell, $l_> = \max(l_i, l_j)$, and $\varepsilon = \omega - E_i$ is the photoelectron energy. E_i is the ionization energy of the ith subshell ($E_i = -\varepsilon_i$) by Koopmans' theorem [79], which is approximately valid in the HFS model. The orbital energy ε_i and the radial wave functions $P_{n_i l_i}(r)$ and $P_{\varepsilon\, l_j}(r)$ are calculated for a given electronic configuration. It should be noted that the XATOM toolkit does not consider orbital hole alignment after ionization by linearly polarized x-ray pulses and hence assumes that the density of bound electrons remains spherically symmetric throughout.

2.1.3 Auger decay

The Auger decay rate that an electron from the jth subshell fills the ith subshell and another electron from the j'th subshell is ejected into the continuum may be written as [68, 80]

$$\Gamma_A(i,jj') = \pi \frac{N_i^H \, N_{jj'}}{2l_i+1} \sum_{L=|l_j-l_{j'}|}^{l_j+l_{j'}} \sum_{S=0}^{1} \sum_{l_{i'}} (2L+1)\,(2S+1)|M_{LS}(j,j',i,i')|^2, \tag{2.6}$$

where i' indicates the continuum state with Auger electron energy $\varepsilon = E_i - E_j - E_{j'}$, N_i^H is the number of the holes in the ith subshell, and

$$N_{jj'} = \begin{cases} \frac{N_j N_{j'}}{(4l_j+2)(4l_{j'}+2)} & \text{for non-equivalent electrons,} \\ \frac{N_j(N_j-1)}{(4l_j+2)(4l_j+2-1)} & \text{for equivalent electrons.} \end{cases} \tag{2.7}$$

Here, averaging schemes over initial and final states to compute transition rates are adopted from Refs. [80, 81, 82]. The matrix element M_{LS} is given as

$$\begin{aligned} M_{LS}(j,j',i,i') = \tau(-1)^{L+l_j+l_{i'}} \sum_K [& R_K(j,j',i,i')A_K(j,j',i,i') \\ & +(-1)^{L+S} R_K(j',j,i,i')A_K(j',j,i,i')], \end{aligned} \tag{2.8}$$

where $\tau = 1/\sqrt{2}$ if j and j' are equivalent electrons and $\tau = 1$ otherwise. A_K is a coefficent related to $3j$ and $6j$ symbols [83],

$$A_K(j,j',i,i') = \langle l_i || C_K || l_j \rangle \, \langle l_{i'} || C_K || l_{j'} \rangle \begin{Bmatrix} l_i & l_{i'} & L \\ l_{j'} & l_j & K \end{Bmatrix}, \tag{2.9}$$

where

$$\langle l||C_K||l'\rangle = \frac{(-1)^l}{\sqrt{(2l+1)(2l'+1)}} \begin{pmatrix} l' & K & L \\ 0 & 0 & 0 \end{pmatrix}, \tag{2.10}$$

and R_K is a double-radial integral defined as

$$\begin{aligned} R_K(j,j',i,i') = \int_0^\infty \int_0^\infty & P_{n_j l_j}(r_1) P_{n_{j'} l_{j'}}(r_2) \frac{r_<^K}{r_>^{K+1}} \\ & \times P_{n_i l_i}(r_1) P_{\varepsilon l_{i'}}(r_2) dr_1 dr_2 \end{aligned} \tag{2.11}$$

2.1.4 Fluorescence

The fluorescence rate for the electric dipole transition of an electron from the jth subshell to a hole in the ith subshell is given by [68, 80]

$$\Gamma_F(i,j) = \frac{4}{3}\alpha^3 (I_i - I_j)^3 \frac{N_i^H N_j}{4l_j+2} \frac{l_>}{2l_i+1} \left| \int_0^\infty P_{n_i l_i}(r) P_{n_j l_j}(r) r dr \right|^2 . \tag{2.12}$$

2.1.5 Coherent x-ray scattering

The coherent x-ray scattering form factor for a given electronic density $\rho(\mathbf{r})$ is given by [68]

$$f^0(\mathbf{Q}) = \int \rho(\mathbf{r}) \mathrm{e}^{\mathrm{i}\mathbf{Q}\cdot\mathbf{r}} \mathrm{d}^3\mathrm{r}, \tag{2.13}$$

where $\mathbf{Q}$ is the photon momentum transfer. Here it is assumed that the atomic electron density is spherically symmetric. Then the atomic form factors depend only on the magnitude of the momentum transfer, so the above Eq. (2.13) can be simplified to

$$f^0(Q) = 4\pi \int_0^\infty r^2 \rho(r) \frac{\sin(Qr)}{Qr} dr, \tag{2.14}$$

where $Q = |\mathbf{Q}| = 2\alpha\omega\sin(\theta/2)$ and θ is the polar angle of the momentum of the scattered photon with respect to the propagation axis of the incoming x rays. For unpolarized x rays, the differential cross section for coherent scattering is given by

$$\frac{d\sigma_S}{d\Omega} = \alpha^4 |f^0(Q)|^2 \frac{1+\cos^2\theta}{2}, \tag{2.15}$$

and for linearly polarized x rays, the differential cross section is given by

$$\frac{d\sigma_S}{d\Omega} = \alpha^4 |f^0(Q)|^2 (1 - \cos^2\phi \sin^2\theta), \tag{2.16}$$

where ϕ is the azimuthal angle of the scattered photon momentum with respect to the x-ray propogation and polarization axes.

2.1.6 Average-atom model

The average-atom model (AA) uses a finite-temperature Hartree-Fock-Slater calculation, which is implemented as an extension of XATOM [58]. AA corresponds to the first step of the two-step model that was used to describe ionization potential depression in dense plasmas [58]. For a single atomic species, the effect of the solid/plasma environment on an electron is taken into account via a muffin-tin-type potential given as

$$V(\mathbf{r}) = \begin{cases} -\frac{Z}{r} + \int_{r' \leq r_s} d^3r' \frac{\rho(\mathbf{r}')}{|\mathbf{r}-\mathbf{r}'|} - \frac{3}{2}\left[\frac{3}{\pi}\rho(\mathbf{r})\right]^{\frac{1}{3}} & \text{for } r \leq r_s \\ V(r_s) & \text{for } r > r_s, \end{cases} \tag{2.17}$$

where Z is the nuclear charge, $\rho(\mathbf{r})$ is the electronic density, and r_s is the Wigner-Seitz radius that is given by the number density n_i of the atomic ions in the solid, using the expression $r_s = (3/(4\pi n_i))^{\frac{1}{3}}$. Using this potential, we solve the effective single-electron Schrödinger equation,

$$\left[-\frac{1}{2}\nabla^2 + V(\mathbf{r})\right]\psi_p(\mathbf{r}) = \varepsilon_p \psi_p(\mathbf{r}), \tag{2.18}$$

where p is a one-particle state index and ε_p is the corresponding orbital energy. The average-atom calculation treats the electronic system using a grand-canonical ensemble. The electronic density then becomes

$$\rho(\mathbf{r}, T) = \sum_p |\psi_p(\mathbf{r})|^2 \tilde{n}_p(\mu, T). \tag{2.19}$$

Here $\tilde{n}_p(\mu, T)$ stands for the fractional occupation numbers given by the Fermi-Dirac distribution at chemical potential μ,

$$\tilde{n}_p(\mu, T) = \frac{1}{e^{(\varepsilon_p - \mu)/T} + 1}. \tag{2.20}$$

In order to ensure charge neutrality, the average number of electrons N_{elec} within the Wigner-Seitz sphere,

$$N_{\text{elec}} = \int_{r \le r_s} d^3r \, \rho(\mathbf{r}, T), \tag{2.21}$$

is fixed to the atomic number Z. Then we obtain μ by solving the following equation:

$$Z - \sum_p \left(\int_{r \le r_s} d^3r |\psi_p(\mathbf{r})|^2 \right) \tilde{n}_p(\mu, T) = 0. \tag{2.22}$$

With the chemical potential μ obtained from Eq. (2.22), one can construct $\rho(\mathbf{r}, T)$ from Eq. (2.19). Using $\rho(\mathbf{r}, T)$, the new updated atomic potential is obtained from

Eq. (2.17). Afterwards, orbitals $\psi_p(\mathbf{r})$ and orbital energies ϵ_p are calculated from Eq. (2.18) using the new potential, and then a new μ is calculated. Thus, orbitals and orbital energies are determined self-consistently until the results are converged. In our calculations, the input parameters are the atomic number Z, the Wigner-Seitz radius r_s via the solid density, and the temperature T of the system.

After completing an average-atom calculation, one obtains the zeroth-order total energy within the Wigner-Seitz sphere (i.e., the total energy per atom),

$$E(T) = \sum_p \varepsilon_p \tilde{n}_p(\mu, T) \int_{r \leq r_s} d^3r \; |\psi_p(\mathbf{r})|^2 \,. \tag{2.23}$$

Within the grand-canonical ensemble, one can calculate the probability distribution of all possible electronic configurations. If we consider a fixed bound-electron configuration $[n_b] = (n_1, \ldots, n_B)$, where B is the number of bound one-electron (spin-orbital) states, then the probability distribution at temperature T is given by

$$P_{[n_b]}(T) = \prod_b^{\text{bound}} \frac{e^{-(\varepsilon_b - \mu) n_b / T}}{1 + e^{-(\varepsilon_b - \mu)/T}}, \tag{2.24}$$

where b runs over all bound states ($1 \leq b \leq B$) and n_b is an integer occupation number (0 or 1) in the bound-electron configuration. Then the charge-state distribution is given by

$$P_Q(T) = \sum_{[n_b]}^{Q} P_{[n_b]}(T), \tag{2.25}$$

where $[n_b]$ runs over all possible bound-state configurations satisfying $\sum_b^{\text{bound}} n_b = Z - Q$.

2.2 XMDYN

2.2.1 Overview

XMDYN [1, 56, 57] has been originally developed for modeling finite-size systems irradiated by an XFEL pulse. It unites a MC description of ionizations with a classical MD treatment of real-space particle dynamics. XMDYN keeps track of the configuration of the bound electrons in neutral atoms and atomic ions individually. These configurations change dynamically because of different atomic processes like inner and outer-shell photoionization, Auger and fluorescence decay and collisional (secondary) ionization and recombination. In order to treat x-ray–atom interactions, XMDYN uses the XATOM toolkit, which is an *ab-initio* framework based on non-relativistic quantum electrodynamics and perturbation theory. XATOM provides rates and cross-sections of x-ray-induced processes such as photoionization, Auger decay and x-ray fluoresence. XMDYN employs XATOM data, keeps track of all the ionization events along with the electron configuration of each atom, calculates impact ionization and recombination and follows the trajectories of all the ionized electrons and atoms, solving the classical equations of motion numerically. The system is propagated with discrete timesteps and snapshots are saved for later analysis.

2.2.2 Molecular Dynamics

Molecular dynamics is a numerical technique to track the real space dynamics of classical particles. The popular Verlet algorithm [84] is used to evaluate the time evolution of a system by integrating the equations of motions. It calculates, for timstep $t + \Delta t$, the coordinates $\mathbf{r}(t + \Delta t)$, velocities $\mathbf{v}(t + \Delta t)$ of all particles from the corresponding values of these quantities at the previous timestep. This algorithm belongs to the class of finite-difference methods. XMDYN uses velocity Verlet algorithm [85], which gives improved accuracy over the Verlet scheme. Equations used in the algorithm are as follows:

$$\mathbf{v}(t+\Delta t/2) = \mathbf{v}(t) + (0.5/m)\,\mathbf{F}(t)\Delta t, \tag{2.26}$$

$$\mathbf{r}(t+\Delta t) = \mathbf{r}(t) + \Delta t\,\mathbf{v}(t+\Delta t/2), \tag{2.27}$$

$$\mathbf{F}(t+\Delta t) = \mathbf{F}(\mathbf{r}(t+\Delta t)), \tag{2.28}$$

$$\mathbf{v}(t+\Delta t) = \mathbf{v}(t+\Delta t/2) + (0.5/m)\,\mathbf{F}(t+\Delta t)\,\Delta t. \tag{2.29}$$

In Eqs. (2.26)- (2.29), m represents the mass of the particle. It can be seen above that the velocity of the system at step $(t+\Delta t/2)$ is calculated first, followed by the calculation at step $(t+\Delta t)$. On the basis of the new coordinates, the potential energy function is evaluated and new forces are determined. One of the key parameters in the above equation is the timestep Δt, which determines how frequently integration is performed. Δt controls the accuracy of the method for the price of the calculation time.

2.2.3 XMDYN code structure

XMDYN is structured into several blocks. A flowchart diagram of XMDYN structure is shown in Fig. 2.2. Within one cycle of the time loop, different blocks are executed accordingly in sequence. Photoionization, Auger and fluorescent relaxation evaluation is performed within the MC-block and the real-space propagation of the classical particles in the MD-block. Electron impact ionization (secondary ionization) and electron recombination occur in the collisional block (CO-block) and recombination block (RE-block), respectively.

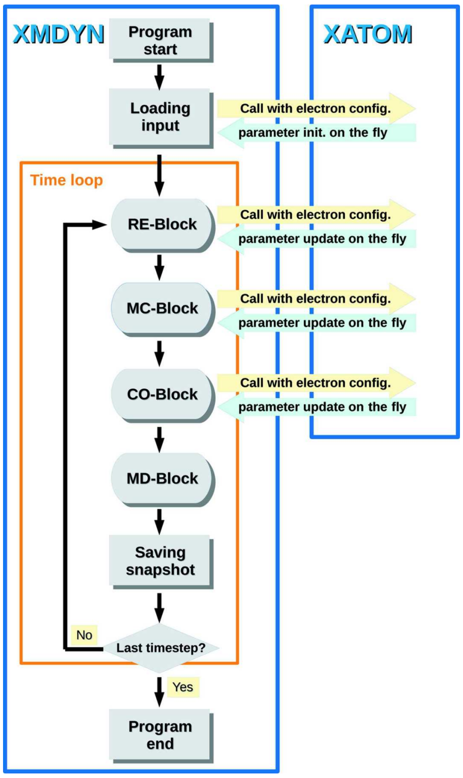
XMDYN
Program start
Loading input
XATOM
Call with electron config.
parameter init. on the fly
Time loop
RE-Block
Call with electron config.
parameter update on the fly
MC-Block
Call with electron config.
parameter update on the fly
CO-Block
Call with electron config.
parameter update on the fly
MD-Block
Saving snapshot
No
Last timestep?
Yes
Program end

FIGURE 2.2: Flowchart of XMDYN, showing the separation and the sequence of different blocks. It also shows on the fly connection with XATOM to calculate various atomic parameters. This figure is taken from Ref. [1].

2.2.4 Monte Carlo block

A Monte Carlo algorithm is used to determine whether an event of a stochastic process such as photoionization, Auger or fluorescent relaxation occurs within a discrete timestep. For each process, the time of occurence is generated randomly at each timestep based on the exponential probability distribution. If a generated value lies within the time interval, the corresponding event happens. Rate and cross-section data parameterize the probability of photoionization, Auger and fluorescent decay. These atomic parameters are calculated with XATOM.

2.2.5 Impact ionization and recombination

Within the XMDYN particle approach, electron impact ionization is not a stochastic process (i.e., no random number is needed in the algorithm), but it depends solely on the real space dynamics (spatial location and velocity) of the particles and on the cross-section. When a classical free electron is close to an atom/ion, its trajectory is extrapolated back to an infinite distance in the potential of the target ion by using energy and angular momentum conservation. Impact ionization occurs only if the impact parameter at infinity is smaller than the radius associated with the total electron impact ionization cross-section. The total cross-section is the sum of the partial cross sections evaluated for the occupied orbitals, using the asymptotic kinetic energy of the impact electron. In the case of an ionization event, the orbital to be ionized is chosen randomly, according to probabilities proportional to the subshell partial cross sections. XMDYN uses the binary-encounter-Bethe (BEB) cross sections [3] supplied with atomic parameters calculated with XATOM. Similarly, in XMDYN, recombination is a process that evolves through the classical dynamics of the particles. The code checks for the ion that has the strongest Coulomb potential for each electron and calculates for how long this condition is fulfilled. Recombination occurs when an electron remains around the same ion for n full periods (e.g., $n = 1$) [86]. While recombination can be identified based on this definition, the electron is still kept classical if its classical orbital energy is higher than the orbital energy of the highest considered orbital i containing a vacancy. When the classical binding becomes stronger, the classical electron is removed and the occupation number of the corresponding orbital is increased by one.

2.2.6 Electron plasma analysis

Electron plasma is formed when electrons are ejected from atoms in ionization events and stay among the ions through an extensive period, e.g. in the bulk. The plasma dynamics are governed not only by the Coulomb interaction between the particles, but also by collisional ionization, recombination, and so on. XMDYN follows the system from the very first photoionization event through non-equilibrium states until thermalization is reached asymptotically. In order to quantify the equilibrium properties reached, we fit the plasma electron velocity distribution using a Maxwell-Boltzmann distribution,

$$f(v) = \sqrt{\left(\frac{1}{2\pi T}\right)^3} 4\pi v^2 e^{-\frac{v^2}{2T}}, \tag{2.30}$$

where T represents the temperature (in units of energy) and v is the electron speed. Atomic units are used unless specified. With the function defined in Eq. (2.30), we fit the temperature, which is used later to compare with equilibrium-state calculations.

2.3 Extensions of XMDYN

In order to extend XMDYN for calculating trajectories for larger systems like nanocrystals of, for example, a biological system like proteins (note that one protein could be calculated), one needs to come up with a strategy that makes the capturing of the dynamics of millions of particles feasible. The dimensions of the interaction volume are defined by the intersection of the x-ray beam and the crystal; therefore its dimensions are determined by the focal area ($\sim\, 100 \times 100\,\mathrm{nm}^2$) and the thickness of the crystal along the beam propagation direction ($\sim\, \mu\mathrm{m}$). The number of atoms within this volume is of the order of 10^9. This number is formidably large – it is not feasible to simulate the whole system by a single XMDYN run. In order to overcome this barrier, the procedure of dividing the whole crystal into smaller units (that are experiencing different fluences because of the spatial beam intensity profile) is proposed. These super-cells may contain several crystallographic unitcells, for which we calculate the dynamics separately using periodic boundary conditions (PBC). For this purpose, I have developed an extension to XMDYN that applies PBC [87, 88] to a super-cell, accounting also for the effect of the environment surrounding it.

2.3.1 Periodic boundary conditions (PBC) using minimum image convention

Within the concept of PBC, a hypothetic crystal is constructed as a periodic extension of a selected super-cell. The total Coulomb interaction energy for a super-cell includes all the interactions within the given cell as well as pair interactions when one particle is in the cell while the other is in a periodic image within the super-cell based hypothetical lattice (PBC-crystal). Formally,

$$E = \frac{1}{4\pi\varepsilon_0}\frac{1}{2}\sum_{\mathbf{n}}\sum_{i=1}^{N}{\sum_{j=1}^{N}}{}' \frac{q_i q_j}{|\mathbf{r}_{ij}+\mathbf{n}L|}, \tag{2.31}$$

where N represents the total number of particles in the super-cell, q_i is the charge of the ith particle, ε_0 is the dielectric constant, L represents the dimension of the cell (here assumed to be a cube), $\mathbf{n}L = n_1\mathbf{c}_1 + n_2\mathbf{c}_2 + n_3\mathbf{c}_3$, where $\mathbf{c}_1, \mathbf{c}_2, \mathbf{c}_3$ represent basis vectors of the PBC-crystal, and n_1, n_2, n_3 are integers indexing the periodic images.

Hence, $|\mathbf{r}_{ij} + \mathbf{n}L|$ is the distance between the ith particle in the central super-cell ($\mathbf{n} = \mathbf{0}$) and the jth particle in the super-cell indexed by $\mathbf{n}$. The symbol $'$ represents the exclusion of the term $j = i$ if and only if $\mathbf{n} = \mathbf{0}$. The summation in Eq. (2.31) is not only computationally very expensive because of the formally infinite sum, but is also conditionally convergent, which states that the result depends upon the order of summation. To overcome this problem, we follow a route used often in the literature for spatially periodic systems – the method of minimum image convention [89]. According to the convention,

1. when evaluating Eq. (2.31), we do not use the same super-cell division of the PBC crystal for all particles, but we always shift the boundaries so that the selected particle appears in the center;
2. we consider only $\mathbf{n} = \mathbf{0}$ terms.

The former choice ensures that no jump happens in the potential energy when a particle crosses a super-cell boundary and therefore 'jumps' in the evaluation from one border of the cell to the opposite. The latter is a minimum choice considering interactions between a selected particle with the closest copy of the others only.

2.3.2 PBC using Ewald summation

This section will provide a useful insight for PBC using Ewald summation [87, 90]. As the summation in Eq. (2.31) is conditionally convergent, therefore using Ewald method, one can evaluate E by transforming it into a summation that converges rapidly and absolutely. The potential field generated by an ion having a charge q_i at a location r_i is given as

$$\phi_i(\mathbf{r}) = \frac{1}{4\pi\varepsilon_0}\frac{q_i}{|\mathbf{r} - \mathbf{r}_i|}. \tag{2.32}$$

The potential field generated by all N ions along with the periodic images using PBC is

$$\phi(\mathbf{r}) = \frac{1}{4\pi\varepsilon_0} \sum_{\mathbf{n}} \sum_{j=1}^{N} \frac{q_j}{|\mathbf{r} - \mathbf{r}_j + \mathbf{n}L|}. \tag{2.33}$$

The potential field generated by all the ions including their images, excluding ion i is given as

$$\phi_{[i]}(r) \equiv \phi(\mathbf{r}) - \phi_i(\mathbf{r}) = \frac{1}{4\pi\varepsilon_0} \sum_{\mathbf{n}} \sum_{j=1}^{N}{}' \frac{q_j}{|\mathbf{r} - \mathbf{r}_j + \mathbf{n}L|}. \tag{2.34}$$

By comparing Eq. (2.31) and Eq. (2.34), we get

$$E = \frac{1}{2} \sum_{i=1}^{N} q_i \phi_{[i]}(\mathbf{r}_i). \tag{2.35}$$

The charge density for a point charge is given as

$$\rho_i(\mathbf{r}) = q_i \delta(\mathbf{r} - \mathbf{r}_i). \tag{2.36}$$

If one considers a more general problem, where all the ions do not necessarily have charge distribution as a delta function, but can spread out in space, then the potential field generated by this charge distribution is the solution of the Poisson's equation:

$$\phi_i(\mathbf{r}) = \frac{1}{4\pi\varepsilon_0} \int \frac{\rho_i(\mathbf{r}')}{|\mathbf{r} - \mathbf{r}'|} d^3\mathbf{r}'. \tag{2.37}$$

The total Coulomb interaction energy E can be written as

$$E = \frac{1}{4\pi\varepsilon_0}\frac{1}{2}\sum_{\mathbf{n}}\sum_{i=1}^{N}\sum_{j=1}^{N}{}' \int\int \frac{\rho_i(\mathbf{r})\rho_j(\mathbf{r}')}{\mathbf{r}-\mathbf{r}'+\mathbf{n}L} d^3\mathbf{r} d^3\mathbf{r}', \tag{2.38}$$

whereas the potential field excluding ion i becomes

$$\phi_{[i]}(\mathbf{r}) = \frac{1}{4\pi\varepsilon_0}\sum_{\mathbf{n}}\sum_{j=1}^{N}{}' \int \frac{\rho_j(\mathbf{r}')}{|\mathbf{r}-\mathbf{r}'+\mathbf{n}L|} d^3\mathbf{r}'. \tag{2.39}$$

If the charge density is given by Eq. (2.36), then Eq. (2.38) and Eq. (2.39) reduce to Eq. (2.31) and Eq. (2.34) respectively.

The charge distribution in our case is described in terms of a delta function. But we can split it into two terms by adding and subtracting a Gaussian distribution:

$$\begin{aligned} \rho_i(\mathbf{r}) &= \rho_i^S(\mathbf{r}) + \rho_i^L(\mathbf{r}) \\ \rho_i^S(\mathbf{r}) &= q_i\delta(\mathbf{r}-\mathbf{r}_i) - q_i G_\sigma(\mathbf{r}-\mathbf{r}_i) \\ \rho_i^L(\mathbf{r}) &= q_i G_\sigma(\mathbf{r}-\mathbf{r}_i), \end{aligned} \tag{2.40}$$

where

$$G_\sigma(\mathbf{r}) = \frac{1}{(2\pi\sigma^2)^{3/2}} \exp\left[-\frac{|\mathbf{r}|^2}{2\sigma^2}\right], \tag{2.41}$$

the standard deviation of the distribution function is given by σ, and S and L represent short-range and long-range terms respectively. Similar to the splitting of the charge, one can split the potential field $\phi_i(\mathbf{r})$ also:

$$\begin{aligned}\phi_i(\mathbf{r}) &= \phi_i^S(\mathbf{r}) + \phi_i^L(\mathbf{r}) \\ \phi_i^S(\mathbf{r}) &= \frac{q_i}{4\pi\varepsilon_0}\int \frac{\delta(\mathbf{r}-\mathbf{r}_i) - G_\sigma(\mathbf{r}-\mathbf{r}_i)}{|\mathbf{r}-\mathbf{r}_i|}\, d^3\mathbf{r}_i \\ \phi_i^L(\mathbf{r}) &= \frac{q_i}{4\pi\varepsilon_0}\int \frac{G_\sigma(\mathbf{r}-\mathbf{r}_i)}{|\mathbf{r}-\mathbf{r}_i|}\, d^3\mathbf{r}_i.\end{aligned} \tag{2.42}$$

Similarly, the potential field generated by all the ions excluding the ith ion can be written as

$$\phi_{[i]}(\mathbf{r}) = \phi_{[i]}^S(\mathbf{r}) + \phi_{[i]}^L(\mathbf{r}). \tag{2.43}$$

Moreover, the Coulomb interaction energy can also be splitted likewise:

$$E = \frac{1}{2}\sum_{i=1}^{N} q_i \phi_{[i]}^S(\mathbf{r}_i) + \frac{1}{2}\sum_{i=1}^{N} q_i \phi_{[i]}^L(\mathbf{r}_i). \tag{2.44}$$

The above equation can also be further splitted by adding and subtracting a self-interaction term:

$$E = \frac{1}{2}\sum_{i=1}^{N} q_i \phi_{[i]}^S(\mathbf{r}_i) + \frac{1}{2}\sum_{i=1}^{N} q_i \phi^L(\mathbf{r}_i) - \frac{1}{2}\sum_{i=1}^{N} q_i \phi_i^L(\mathbf{r}_i) \tag{2.45}$$

$$E^S = \frac{1}{2}\sum_{i=1}^{N} q_i \phi_{[i]}^S(\mathbf{r}_i) \tag{2.46}$$

$$E^L = \frac{1}{2}\sum_{i=1}^{N} q_i \phi^L(\mathbf{r}_i) \tag{2.47}$$

$$E^{self} = -\frac{1}{2}\sum_{i=1}^{N} q_i \phi_i^L(\mathbf{r}_i). \tag{2.48}$$

The potential field due to the Gaussian charge distribution can be obtained using Poisson's equation:

$$\nabla^2\phi_\sigma(\mathbf{r}) = -\frac{G_\sigma(\mathbf{r})}{\varepsilon_0}. \tag{2.49}$$

Solving the above equation, we get

$$\phi_\sigma(\mathbf{r}) = \frac{1}{4\pi\varepsilon_0|\mathbf{r}|}\,\mathrm{erf}\left(\frac{|\mathbf{r}|}{\sqrt{2}\sigma}\right). \tag{2.50}$$

Therefore,

$$\phi_i^S(\mathbf{r}) = \frac{1}{4\pi\varepsilon_0}\frac{q_i}{|\mathbf{r}-\mathbf{r}_i|}\,\mathrm{erfc}\left(\frac{|\mathbf{r}-\mathbf{r}_\mathrm{i}|}{\sqrt{2}\sigma}\right) \tag{2.51}$$

$$\phi_i^L(\mathbf{r}) = \frac{1}{4\pi\varepsilon_0}\frac{q_i}{|\mathbf{r}-\mathbf{r}_i|}\,\mathrm{erf}\left(\frac{|\mathbf{r}-\mathbf{r}_\mathrm{i}|}{\sqrt{2}\sigma}\right). \tag{2.52}$$

Here, $\phi_i^L(\mathbf{r})$ is a long-range non-singular potential and $\phi_i^S(\mathbf{r})$ is a short-range singular potential. Excluding the contribution from the ith ion, the potential can be rewritten as

$$\phi_{[i]}^S(\mathbf{r}) = \frac{1}{4\pi\varepsilon_0}\sum_{\mathbf{n}}\sum_{j=1}^{N}{}'\frac{q_j}{|\mathbf{r}-\mathbf{r}_j+\mathbf{n}L|}\,\mathrm{erfc}\left(\frac{|\mathbf{r}-\mathbf{r}_\mathrm{j}+\mathbf{n}\mathrm{L}|}{\sqrt{2}\sigma}\right). \tag{2.53}$$

Similarly, the short-range term Eq. (2.46) of the Coulomb interaction energy can be written as

$$E^S = \frac{1}{2}\frac{1}{4\pi\varepsilon_0}\sum_{\mathbf{n}}\sum_{i=1}^{N}\sum_{j=1}^{N}{}'\frac{q_iq_j}{|\mathbf{r}_i-\mathbf{r}_j+\mathbf{n}L|}\,\mathrm{erfc}\left(\frac{|\mathbf{r}_\mathrm{i}-\mathbf{r}_\mathrm{j}+\mathbf{n}\mathrm{L}|}{\sqrt{2}\sigma}\right). \tag{2.54}$$

The above equation differs from the total Coulomb interaction energy E due to the erfc term, which truncates the potential function at large distances. Therfore, E^S

can be computed from the sum in real space, controlling the error by introducing a finite cutoff. As we have the expression Eq. (2.52) for the long-range potential, therefore the self energy term can be computed as follows:

$$\phi_i^L(\mathbf{r}_i) = \frac{q_i}{4\pi\varepsilon_0}\sqrt{\frac{2}{\pi}}\frac{1}{\sigma} \tag{2.55}$$

$$E^{self} = -\frac{1}{4\pi\varepsilon_0}\frac{1}{\sqrt{2\pi}\sigma}\sum_{i=1}^{N} q_i^2. \tag{2.56}$$

$\phi^L(\mathbf{r})$ represents the potential field generated by a periodic array of ions, which includes the contributions from all the ions. The total charge density field is a periodic function and is given as:

$$\rho^L(\mathbf{r}) = \sum_{\mathbf{n}}\sum_{i=1}^{N} \rho_i^L(\mathbf{r} + \mathbf{n}L). \tag{2.57}$$

Therefore, $\phi^L(\mathbf{r})$ can be Fourier transformed into its reciprocal space:

$$\hat{\phi}^L(\mathbf{k}) = \int_V \phi^L(\mathbf{r})\, \exp(-i\mathbf{k}\cdot\mathbf{r})\, d^3\mathbf{r} \tag{2.58}$$

$$\hat{\rho}^L(\mathbf{k}) = \int_V \rho^L(\mathbf{r})\, \exp(-i\mathbf{k}\cdot\mathbf{r})\, d^3\mathbf{r}, \tag{2.59}$$

where $\hat{\phi}^L(\mathbf{k})$ and $\hat{\rho}^L(\mathbf{k})$ are the Fourier transforms of $\phi^L(\mathbf{r})$ and $\rho^L(\mathbf{r})$ respectively. Reciprocal vector is represented by $\mathbf{k}$. In order to compute E^L, first the Fourier transform of the charge density is calculated. Then the long-range potential in real space is calculated by using its inverse Fourier transform. Hence the potential becomes

$$\phi^L(\mathbf{r}) = \frac{1}{V\,\varepsilon_0}\sum_{k\neq 0}\sum_{j=1}^{N}\frac{q_j}{k^2}\, \exp(i\mathbf{k}\cdot(\mathbf{r}-\mathbf{r}_j))\, \exp(-\sigma^2 k^2/2), \tag{2.60}$$

where $k = |\mathbf{k}|$. The contribution to the $k = 0$ term is zero as the supercell is charge neutral, i.e. $\sum_{i=1}^{N} q_i = 0$. Therefore,

$$E^L = \frac{1}{V\,\varepsilon_0} \sum_{k \neq 0} \sum_{i=1}^{N} \sum_{j=1}^{N} \frac{q_i q_j}{k^2} \, \exp(i\mathbf{k} \cdot (\mathbf{r}_i - \mathbf{r}_j)) \, \exp(-\sigma^2 k^2 / 2). \tag{2.61}$$

Hence, the final equation can be written as

$$E = E^S + E^L + E^{self},$$

or equivalently

$$\begin{aligned} E = \frac{1}{2} \frac{1}{4\pi\varepsilon_0} \sum_{\mathbf{n}} \sum_{i=1}^{N} {\sum_{j=1}^{N}}' \frac{q_i q_j}{|\mathbf{r}_i - \mathbf{r}_j + \mathbf{n}L|} \operatorname{erfc}\left(\alpha |\mathbf{r}_{\mathrm{i}} - \mathbf{r}_{\mathrm{j}} + \mathbf{n}\mathrm{L}|\right) + \\ \frac{1}{V\,\varepsilon_0} \sum_{k \neq 0} \sum_{i=1}^{N} \sum_{j=1}^{N} \frac{q_i q_j}{k^2} \, \exp(i\mathbf{k} \cdot (\mathbf{r}_i - \mathbf{r}_j)) \, \exp(-k^2 / 4\,\alpha^2) - \\ \frac{1}{4\pi\varepsilon_0} \frac{\alpha}{\sqrt{\pi}} \sum_{i=1}^{N} q_i^2. \end{aligned} \tag{2.62}$$

In the above Eq. (2.62), α represents the Ewald splitting parameter and is given as $\alpha = 1/\sqrt{2}\,\sigma$. In practice, the sum over E^S and E^L are computed considering cutoffs given by $\mathrm{R}_{\mathrm{cut}} = \theta(\sigma)$ for real-space contribution and $\mathrm{K}_{\mathrm{cut}} = \theta(\alpha)$ for k-space. Optimal value for α parameter should be considered in order to make Ewald summation computationally inexpensive. In general one chooses α large enough so one can employ minimum image convention in Eq. (2.54). The inverse length α, which is also known as the splitting parameter, tunes the relative weights of the real- and the reciprocal-space contributions. The cutoffs $\mathrm{R}_{\mathrm{cut}}$ and $\mathrm{K}_{\mathrm{cut}}$ are optimized with respect to α such that the required computer time scales like $N^{3/2}$ as given in Ref. [91].

TABLE 2.1: CPU timings for 1000 particles

α (1/Å)	R_{cut}	K_{cut}	**CPU R-space timing**		**CPU K-space timing**	
			Potential (sec)	**Force** (sec)	**Potential** (sec)	**Force** (sec)
1.0	1	25	0.885	3.1825	12.2903	10356.6
0.2	1	6	0.885	3.1825	0.1996	176.108
0.05	3	1	45.567	76.827	0.0022	2.1467
0.025	5	1	208.51	325.04	0.0022	2.1467
0.0125	10	1	1222.8	2057.4	0.0022	2.1467

TABLE 2.2: GPU timings for 1000 particles

α (1/Å)	R_{cut}	K_{cut}	**GPU R-space timing**		**GPU K-space timing**	
			Potential (sec)	**Force** (sec)	**Potential** (sec)	**Force** (sec)
1.0	1	25	1.109	0.054	12.29	125.9
0.2	1	6	1.129	0.053	0.199	2.096
0.05	3	1	2.332	0.582	0.002	0.0324
0.025	5	1	6.103	2.225	0.002	0.0324
0.0125	10	1	36.51	15.36	0.002	0.0324

However, it is required that $R_{cut} > \mathrm{length}/2$ restricting the minimum image convention in the real-space. For given finite real- and reciprocal-space cutoffs there exists an optimal α value such that the accuracy of the approximated Ewald summation is the highest possible. The optimal value can be determined easily with the help of the estimates for the cutoff errors given in Ref. [87], which essentially is done by demanding that the real- and reciprocal-space contribution to the error should be equal. The computational cost using Ewald summation and minimum image convention are given in Table 2.1

2.3.3 Construction of a nanocrystal

Finally, one can assemble the entire real crystal from the individually simulated super-cells to model the whole dynamics. While in this way, modeling becomes feasible even without the need of supercomputers, we should also note a shortcoming of this approach: we do not allow particle transport, in particular electron transport between the super-cells. For biologically relevant light elements, Auger and secondary electrons have energies $E_{kin} \lesssim 300\,\mathrm{eV}$, which yield a short mean free path in a dense environment. Therefore, such electrons may travel only to neighboring super-cells experiencing similar fluences during the irradiation, so that the effect of net transport may be negligible. On the other hand, photoelectrons have an energy almost as high as the photon energy. Hence, they are fast and have a long mean free path. They can leave super-cells located at high-fluence regions and can affect super-cells at larger distances experiencing lower fluences. We will overcome this shortcoming of the model in the future. Both of the approaches explained in Sec. 2.3 are implemented in XMDYN. I only choose minimum image convention rather than Ewald summation in our simulations as it is computationally less expensive.

Chapter 3

Radiation damage in solid-density matter

This chapter is centered on a publication [2] that is based on the theoretical framework explained in Chapter 2. In order to have a theoretical insight into the calculation of the scattering patterns from a nanocrystal, one needs to investigate the radiation damage in nanocrystals exposed to intense x-ray pulses. Therefore, the non-equilibrium evolution of the warm-dense plasma towards the equilibrium state needs to be analyzed.

3.1 A molecular-dynamics approach for studying thermalization properties of x-ray-heated solid-density matter

3.1.1 Motivation

When matter is exposed to a high-intensity x-ray free-electron-laser pulse, the x rays excite inner-shell electrons leading to the ionization of the electrons through various atomic processes and creating high-energy-density plasma, i.e., warm or hot dense matter. The resulting system consists of atoms in various electronic configurations, thermalizing on sub-picosecond to picosecond timescales after photoexcitation. I present a simulation study of x-ray-heated solid-density matter. For this, I use XMDYN, a Monte-Carlo molecular-dynamics-based code with periodic boundary conditions, which allows one to investigate non-equilibrium dynamics. XMDYN is capable of treating systems containing light and heavy atomic species with full electronic configuration space and 3D spatial inhomogeneity. For the validation of the approach, I compare for a model system the electron temperatures and the ion charge-state distributions from XMDYN to results for the thermalized system based on the AA model implemented in XATOM. Furthermore, I compare the average charge evolution of diamond with the predictions of a Boltzmann continuum approach. I demonstrate that XMDYN results are in good quantitative agreement with the above mentioned approaches, suggesting that the current implementation of XMDYN is a viable approach to simulate the dynamics of x-ray-driven non-equilibrium dynamics in solids. In order to illustrate the potential of XMDYN for treating complex systems, I present calculations on the triiodo benzene derivative 5-amino-2,4,6-triiodoisophthalic acid (I3C), a compound of relevance to biomolecular imaging, consisting of heavy and light atomic species.

3.1.2 Molecular dynamics with super-cell approach

My focus here is the bulk properties of highly excited matter. XMDYN uses the concept of periodic boundary conditions (PBC) to simulate bulk behavior [64, 5]. In the PBC concept, I calculate the irradiation-induced dynamics of a smaller unit, called a super-cell. A hypothetical, infinitely extended system is constructed as a periodic extension of the super-cell. The driving force of the dynamics, the Coulomb interaction, is then calculated for all the particles inside the super-cell within the minimum image convention [89]. Therefore, the total Coulomb force acting on a charge is given by the interaction with other charges within its well-defined neighborhood containing also particles of the surrounding copies of the super-cell.

While core-excited states of atoms decay typically within a few femtoseconds, electron impact ionization and recombination events occur throughout the thermalization process and are in dynamical balance in thermal equilibrium.

3.2 Validation of the methodology

I first consider a model system consisting of carbon atoms. For a reasonable comparison of the results from XMDYN and AA, one should choose a system that can be addressed using both tools. AA does not consider any motion of atomic nuclei. Therefore, I had to restrict the translational motion of atoms and atomic ions in XMDYN simulations as well. In order to do so, I set the carbon mass artificially so large that atomic movements were negligible throughout the calculations. Furthermore, I increased the carbon-carbon distances to reduce the effect of the neighboring ions on the atomic electron binding energies. In XMDYN simulations, I chose a super-cell of 512 carbon atoms arranged in a diamond structure, but with a 13.16 Å lattice constant (in case of diamond, it is 3.567 Å). The number density of the carbon atoms is $\rho_0 = 3.5 \times 10^{-3}\text{Å}^{-3}$, which corresponds to a mass density of $0.07\mathrm{g/cm^3}$. Plasma is generated by choosing different irradiation conditions typical at XFELs. Three different fluences, $\mathcal{F}_{\text{low}} = 6.7\times10^{9}\,\mathrm{ph}/\mu\mathrm{m}^2$, $\mathcal{F}_{\text{med}} = 1.9\times10^{11}\,\mathrm{ph}/\mu\mathrm{m}^2$, and $\mathcal{F}_{\text{high}} = 3.8\times10^{11}\,\mathrm{ph}/\mu\mathrm{m}^2$, are considered. In all the three cases, the photon energy and pulse duration are 1 keV and 10 fs (full width at half maximum), respectively.

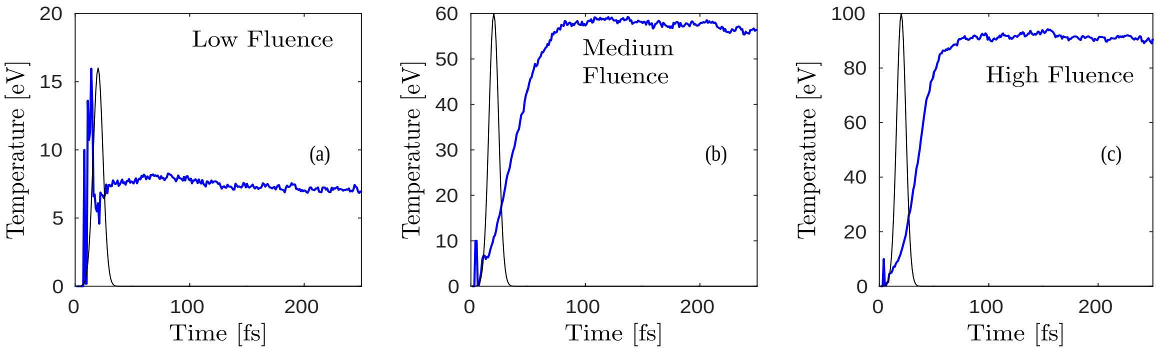

FIGURE 3.1: Time evolution of the temperature of the electron plasma within XMDYN simulation during and after x-ray irradiation at different fluences: (a) $\mathcal{F}_{\text{low}} = 6.7\times10^{9}$ ph/μm^2, (b) $\mathcal{F}_{\text{med}} = 1.9\times10^{11}$ ph/μm^2 and (c) $\mathcal{F}_{\text{high}} = 3.8\times10^{11}$ ph/μm^2. In all three cases, the pulse duration is 10 fs FWHM; the pulse is centered at 20 fs, and the photon energy is 1 keV. The black curve represents the gaussian temporal envelope. Note that in all cases, equilibrium is reached within 100 fs after the pulse. This figure is taken from Ref. [2].

From XMDYN plasma simulations shown in Fig. 3.1, the time evolution of the temperature of the electron plasma is analyzed by fitting to Eq. (2.32). Counterintuitively, right after photon absorption has finished, the temperature is still low, and then it gradually increases, although no more energy is pumped into the system. The reason is that during the few tens of femtoseconds' irradiation, the fast photoelectrons are not yet part of the free electron thermal distribution. Initially, only the low-energy secondary electrons and Auger electrons that have lost a significant part of their energy in collisions determine the temperature. The fast electrons thermalize on longer timescales as shown in Figs. 3.1(b) and (c), contributing to the equilibrated subset of electrons. In all cases, equilibrium is reached within 100 fs after the pulse.

AA calculates only the equilibrium properties of the system, which means that it does not consider the history of the system's evolution through non-equilibrium states. I first calculate the total energy per atom, $E(T)$, as a function of temperature

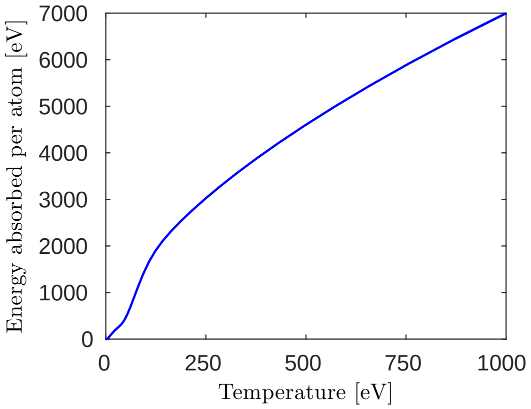

FIGURE 3.2: Relation between plasma temperature and energy absorbed per atom in AA calculations for a carbon system of mass density $0.07\mathrm{g/cm}^3$. This figure is taken from Ref. [2].

T within a carbon system of density ρ_0:

$$E(T) = \sum_p \varepsilon_p \tilde{n}_p(\mu, T) \int_{r \le r_s} d^3r \, |\psi_p(\mathbf{r})|^2 \,, \tag{3.1}$$

where p is a one-particle state index, ε_p and ψ_p are the corresponding orbital energy and orbital respectively, and $\tilde{n}_p$ stands for the fractional occupation number at chemical potential μ. Details are found in Ref. [58]. In this way, I obtain a relation between the average energy absorbed per atom, $\Delta E = E(T) - E(0)$, and the electron temperature (see Fig. 3.2). From XMDYN, the average number of photoionization events per atom, n_{ph}, is available for each fluence point, and therefore the energy absorbed on an average by an atom is known (= $n_{\mathrm{ph}} \times \omega_{\mathrm{ph}}$, where ω_{ph} is the photon energy). Using this value, I can select the corresponding temperature that AA yields. This temperature is compared with that fitted from XMDYN simulations. All these results are in reasonable agreement, as shown in Table 3.1. Later, I use this temperature for calculating the charge-state distributions.

Figure 3.3 shows the kinetic-energy distribution of the electron plasma (in the

Parameters	Low fluence	Medium fluence	High fluence
Fluence (ph/μm^2)	6.7×10^9	1.9×10^{11}	3.8×10^{11}
Energy absorbed per atom (eV)	29	665	1170
XMDYN temperature (eV)	7	57	91
AA temperature (eV)	6	60	83

TABLE 3.1: Final temperatures obtained from XMDYN runs after 250 fs propagation and from AA calculations. XMDYN temperatures are obtained from fitting using Eq. (2.32), while AA temperatures are obtained from the absorbed energy–temperature relation (Fig. 3.2). This table is taken from Ref. [2].

left panels) and the charge-state distributions (in the right panels) for the three different fluences. The charge-state distributions obtained from XMDYN at the final timestep (250 fs) are compared to those obtained from AA at the temperatures specified in Table 3.1. Although similar charge states are populated using the two approaches, differences can be observed: AA yields consistently higher ionic charges than XMDYN (20%–30% higher average charges) for the cases investigated.

This is probably for the following reasons. XMDYN calls XATOM on the fly to calculate re-optimized orbitals for each electronic configuration. In this way, XMDYN accounts for the fact that ionizing an ion of charge Q costs less energy than ionizing an ion of charge $(Q+1)$. However, in the current implementation of AA, this effect is not considered. At a given temperature, AA uses the same orbitals (and therefore the same orbital energies) irrespective of the charge state. A likely consequence is that AA gives more population to higher charge states, simply because their binding energies are underestimated. That could also be the reason why

AA produces wider charge-state distributions and predicts a somewhat higher average charge than XMDYN does. The other reason for the discrepancies could be the fact that XMDYN treats only those orbitals as being quantized that are occupied in the ground state of the neutral atom. For carbon, these are the $1s, 2s$, and $2p$ orbitals. All states above are treated classically in XMDYN, resulting in a continuum of bound states. As a consequence, the density of states is different and it may yield different orbital populations and therefore different charge-state distributions. Moreover, while free-electron thermalization has been ensured, the bound electrons are not necessarily fully thermalized in XMDYN. In spite of the discrepancies observed, XMDYN and AA equilibrium properties are in reasonably good agreement.

I also performed simulations under the conditions that had been used in a recent publication using a continuum approach [4]. In these simulations, nuclear motions are not restricted. A Gaussian x-ray pulse of 10 fs FWHM was used. The intensities considered lie within the regime typically used for high-energy-density experiments : $I_{\rm max} = 10^{16}\,{\rm W/cm^2}$ for $\omega_{\rm ph}$ = 1000 eV, and $I_{\rm max} = 10^{18}\,{\rm W/cm^2}$ for $\omega_{\rm ph}$ = 5000 eV. I employed a super-cell of diamond (mass density = $3.51\,{\rm g/cm^3}$) containing 1000 carbon atoms within the PBC framework. In this study, 25 different Monte-Carlo realizations were calculated and averaged for each irradiation case in order to improve the statistics of the results. For a system of 1000 carbon atoms, each XMDYN trajectory takes 45 minutes of runtime on Intel (R) Xeon (R) CPU E5-2609 @ 2.40 GHz. The average energy absorbed per atom [Fig. 3.4] is $\sim 28\,$eV and $\sim 26\,$eV, respectively, for the 1000-eV and 5000-eV photon-energy cases, in agreement with Ref. [4]. Figure 3.5 shows the time evolution of the average charge for the two different photon energies. Average atomic charge states of +1.1 and +0.9, respectively, were obtained long after the pulse was over. Although the rapid increase of the

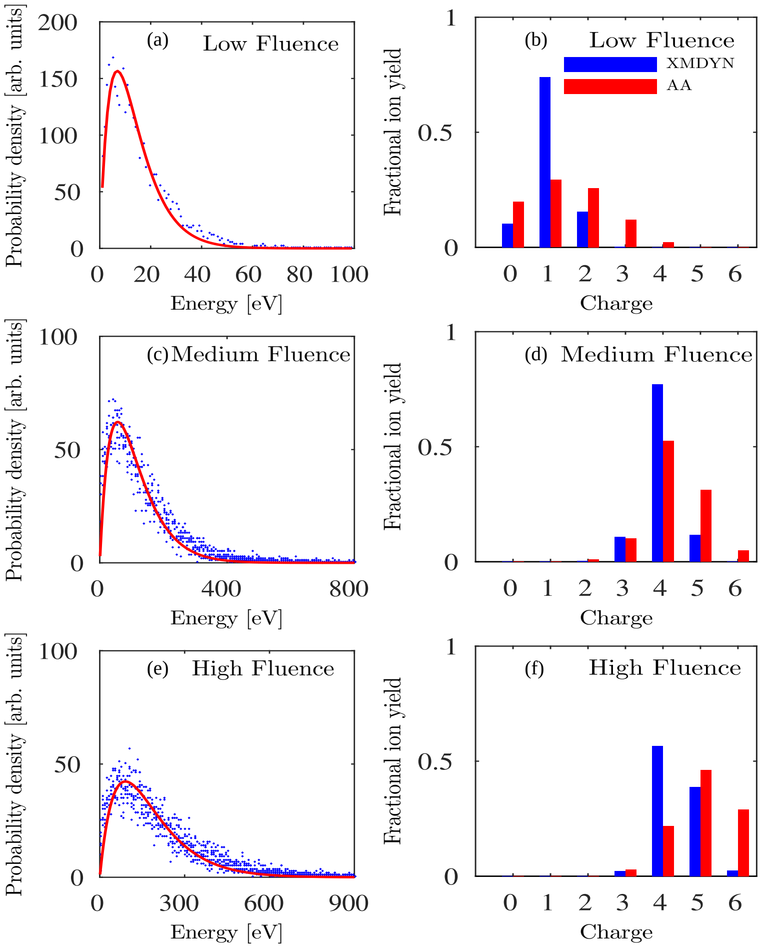

FIGURE 3.3: Kinetic-energy distribution of the electron plasma and charge-state distributions from AA and XMDYN simulations (250 fs after the irradiation) for low fluence (a,b), medium fluence (c,d), and high fluence (e,f). This figure is taken from Ref. [2].

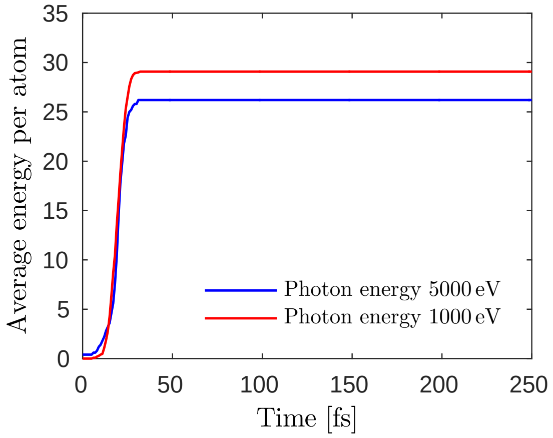

FIGURE 3.4: Average energy absorbed per atom within diamond irradiated with a Gaussian pulse of hard and soft x rays of ω_{ph} = 5000 eV, $I_{\max} = 10^{18}\,\mathrm{W/cm^2}$ and ω_{ph} = 1000 eV, $I_{\max} = 10^{16}\,\mathrm{W/cm^2}$, respectively. In both cases, a pulse duration of 10 fs FWHM was used. This figure is taken from Ref. [2].

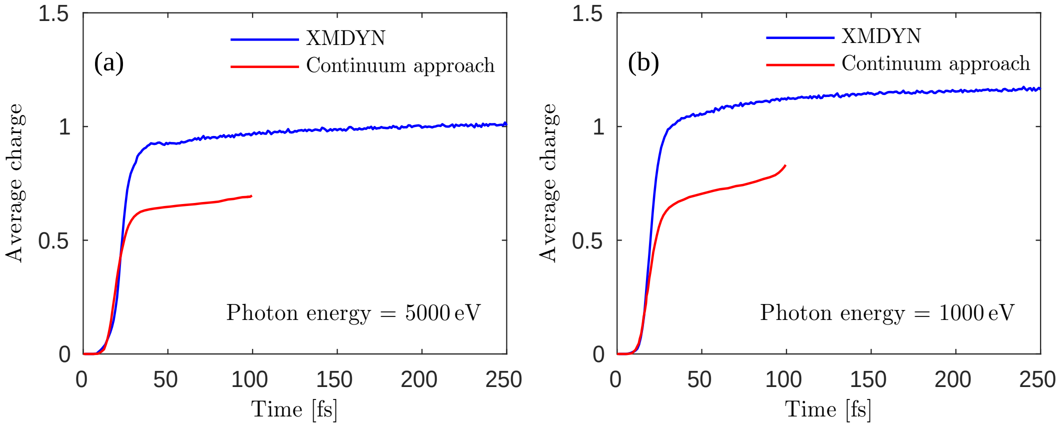

FIGURE 3.5: Average charge within diamond irradiated with a Gaussian pulse of hard and soft x rays of (a) ω_{ph} = 5000 eV, $I_{\max} = 10^{18}\,\mathrm{W/cm^2}$ and (b) ω_{ph} = 1000 eV, $I_{\max} = 10^{16}\,\mathrm{W/cm^2}$, respectively. In both cases, a pulse duration of 10 fs FWHM was used. This figure is taken from Ref. [2].

average ion charge is happening on very similar times, the charge values at the end of the calculation are 30% and 40% higher than those in Ref. [4] for the 1000-eV and 5000-eV cases, respectively [Fig. 3.5(a,b)].

I can name two reasons that can cause such differences in the final charge states. One is that two different formulae for the total impact ionization cross section were used in the two approaches. In Ref. [4], the cross sections are approximated from experimental ground state atomic and ionic data [92], while XMDYN employs the semi-empirical BEB formula taking into account state-specific properties. Figure 3.6 compares these cross sections for neutral carbon atom. It can be seen that the cross section and, therefore, the rate of the ionization used by XMDYN are larger, which can shift the final average charge state higher as well. The second reason is the evaluation of the three-body recombination cross section. In Ref. [4], recombination is defined using the principle of microscopic reversibility, which states that the cross section of impact ionization can be used to calculate the recombination rate [93]. In the current implementation of the Boltzmann code, the two-body distribution function is approximated using one-body distribution functions in the evaluation of the rate for three-body recombination, whereas in XMDYN, correlations at all levels are naturally captured within the classical framework due to the explicit calculation of the microscopic electronic fields. Besides the fundamental differences in the two approaches, one can see a good agreement between the final average charge states.

3.3 Application

In order to demonstrate the capabilities of XMDYN, I investigate the complex system of crystalline form I3C (chemical composition: $C_8H_4I_3NO_4 \cdot H_2O$) [94] irradiated by intense x rays. I3C contains the heavy atomic species iodine, which makes

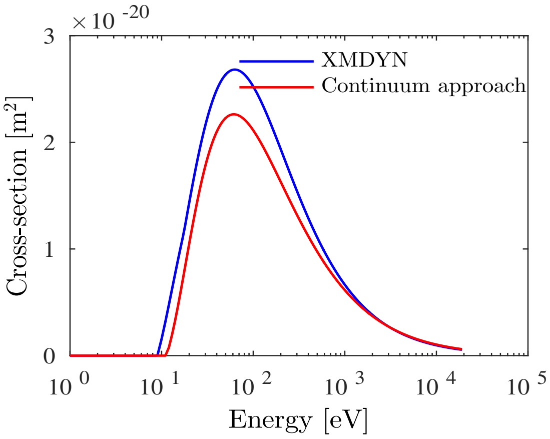

FIGURE 3.6: Comparison of impact ionization cross sections for neutral ground-state carbon atom used in the current work within XMDYN based on the BEB formula [3], and the cross sections used in the continuum approach of Ref. [4] based on experimental data. This figure is taken from Ref. [2].

it a good prototype for investigations of experimental phasing methods based on anomalous scattering [33, 34, 35, 36, 37, 38]. I considered pulse parameters used at an imaging experiment recently performed at the Linac Coherent Light Source (LCLS) free-electron laser [95]. The photon energy was 9.7 keV and the pulse duration was 10 fs FWHM. Two different fluences were considered in the simulations, $\mathcal{F}_{\text{high}} = 1.0 \times 10^{13}\,\text{ph}/\mu\text{m}^2$ (estimated to be in the center of the focus) and its half value $\mathcal{F}_{\text{med}} = 5.0 \times 10^{12}\,\text{ph}/\mu\text{m}^2$. In these simulations, I do not restrict nuclear motions.

The computational cell used in the simulations contained 8 molecules of I3C (184 atoms in total). The time propagation ends 250 fs after the pulse. For the analysis, 50 XMDYN trajectories are calculated for both the fluence cases. These trajectories sample the stochastic dynamics of the system without any restriction of the electronic configuration space that possesses $(2.0 \times 10^7)^{24}$ possible configurations, considering the subsystem of the 24 iodine atoms only. The calculation of such an XMDYN trajectory takes approximately 150 minutes on a Tesla M2090 GPU, while the same calculation takes 48 hours on Intel Xenon X5660 2.80GHz CPU (single core).

Figure 3.7 shows the average charge for the different atomic species in I3C as a function of time. Both fluences pump enormous energy in the system predominantly through the photoionization of the iodine atoms due to their large photoionization cross section. In both the cases, almost all the atomic electrons are removed from the light atoms, but mainly via secondary ionization. The ionization of iodine is very efficient; when applying the weaker fluence $\mathcal{F}_{\mathrm{med}}$, the iodine atoms already lose on average roughly half of their electrons, whereas for the high fluence case, the average atomic charge goes even above +40. Furthermore, I investigate the free electron thermalization. The plasma electrons reach thermalization via non-equilibrium evolution within approximately 200 fs. The Maxwellian distribution of the kinetic energy of these electrons corresponds to very high temperatures: 365 eV for $\mathcal{F}_{\mathrm{med}}$ and 1 keV for $\mathcal{F}_{\mathrm{high}}$ (see Fig. 3.8). Hence, we have shown that XMDYN is a tool that can treat systems with 3D spatial inhomogeneity, whereas the continuum models usually deal with uniform or spherically symmetric samples. If the sample includes heavy atomic species, pre-selecting electronic configurations can affect the dynamics of the system. XMDYN allows for a flexible treatment of the atomic composition of the sample and, particularly, easy access to the electronic structure of heavy atoms with large electronic configuration space.

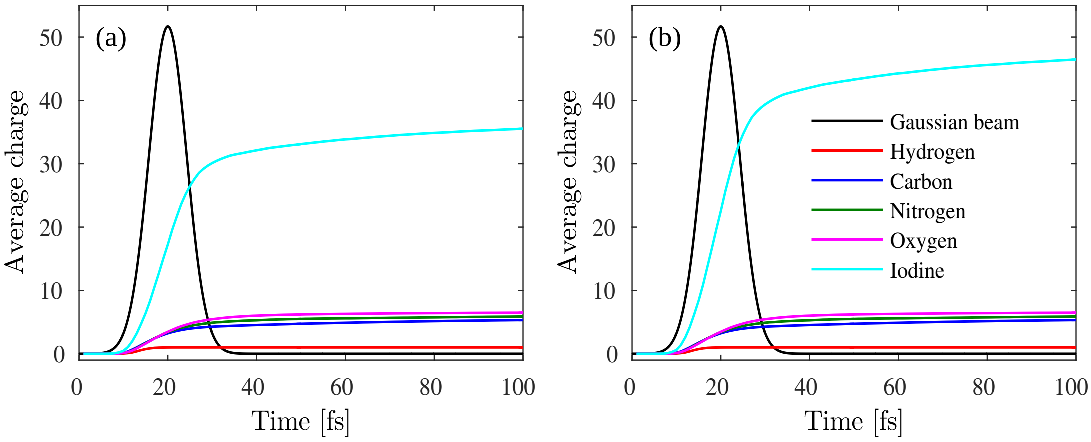

FIGURE 3.7: Average atomic charge in I3C as a function of time for (a) $\mathcal{F}_{\text{med}} = 5.0 \times 10^{12}\,\text{ph}/\mu\text{m}^2$ and (b) $\mathcal{F}_{\text{high}} = 1.0 \times 10^{13}\,\text{ph}/\mu\text{m}^2$, respectively. In both cases, a pulse duration of 10 fs FWHM was used. The photon energy was 9.7 keV. This figure is taken from Ref. [2].

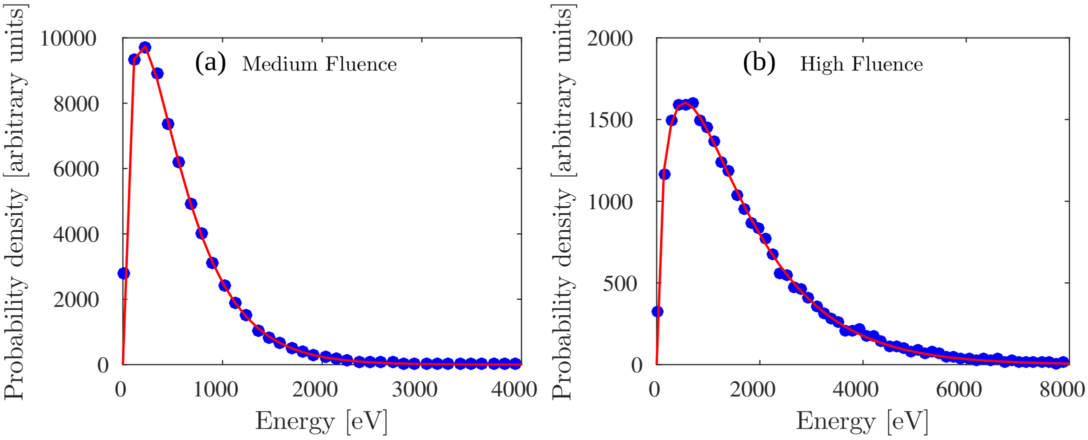

FIGURE 3.8: Kinetic-energy distribution of the electron plasma in I3C from XMDYN simulations (250 fs after the irradiation) for the medium fluence (a) and the high fluence (b). This figure is taken from Ref. [2].

Chapter 4

XSINC: X-ray scattering in nanocrystals

In this chapter, following a publication [5], I present a generalized method to describe the x-ray scattering intensity of the Bragg spots in a diffraction pattern from nanocrystals exposed to intense x-ray pulses. The methodology involves the subdivision of a crystal into smaller units. In order to calculate the dynamics within every unit cell, XMDYN hybrid framework using real space periodic boundary conditions is employed. By combining all the units, I simulate the diffraction pattern of a crystal larger than the transverse x-ray beam size, a situation commonly encountered in femtosecond nanocrystallography experiments with focused x-ray free-electron laser radiation. The last section is also based on a publication [6], which describes a precise construction of the effective form factors for the reconstruction of protein structures.

4.1 Calculation of x-ray scattering patterns from nanocrystals at high x-ray intensity

4.1.1 Motivation

For imaging nano size sample of proteins and viruses at atomic resolution, one calls for high intensity and short x-ray pulses. The shortcoming of high intensities is the rapid ionization of the atoms on the few femtosecond timescale, which affects the structure of the system. This radiation-induced damage changes the atomic form factors and may induce significant atomic displacement on longer times. Finally, radiation damage changes the scattering pattern. The bottleneck one faces is that it is computationally not feasible to simulate a system with realistic (e.g. micrometer) size using software tools that are capable of following the dynamics of each atom, required for imaging studies. Here, I present a methodology to overcome this computational bottleneck.

4.1.2 Methodology of simulating scattering pattern

For a comprehensive theoretical study of signal formation in an SFX experiment, one needs to simulate

(i) the radiation-induced dynamics of the sample and

(ii) the pattern formation based on the dynamics.

In the theoretical study presented here, I consider a micron-sized crystal in a 100 nm focus beam, a scenario where a nanocrystalline sample experiences fluences as high as those typically used in single-particle imaging experiments. As a consequence, the x-ray fluence is non-uniform throughout the sample. This may also have its imprint on the scattering pattern. However, it is computationally not feasible to simulate a system with realistic size while following the dynamics of each atom, required for imaging studies. Therefore, I present an approach that involves the divison of a crystal into smaller units (super-cells) and the calculation of their dynamics individually using periodic boundary conditions (PBC). In order to investigate the effect of inhomogeneous spatial fluence distribution, the super-cells are subjected to different fluences. Then, combining all the super-cells, a nano-crystal is formed and the scattering pattern is constructed under the influence of uniform (within the irradiated part of the sample) and non-uniform spatial beam profiles.

4.1.3 Super-cell approach for scattering signal evaluation

The dimensions of the interaction volume are defined by the intersection of the x-ray beam and the crystal. Therefore, its dimensions are determined by the focal area ($\sim 100 \times 100\,\mathrm{nm}^2$) and the thickness of the crystal along the beam propagation direction ($\sim \mu\mathrm{m}$). The number of atoms within this volume is of the order of 10^9. This number is formidably large; it is not feasible to simulate the whole system by a single XMDYN run. In order to overcome this barrier, a procedure of dividing the whole crystal into smaller units is employed. These super-cells may contain several crystallographic unit cells. The dynamics within each super-cell driven by the local fluence (assumed to be uniform throughout the super-cell) individually is followed. For this purpose, an extension to XMDYN is used that applies PBC [87, 88] to a super-cell, accounting also for the effect of the environment surrounding it.

Scattering intensity

Although, during a single shot experiment, the sample may undergo significant changes, the scattering patterns are static. They accumulate diffracted signal over the whole pulse. Further, the signal may contain an imprint of a spatially non-uniform intensity profile. Formally, the scattering intensity at a specific reflection described by the reciprocal vector **Q**, including the integration over time and the subdivision of the crystal volume into super-cells, according to the approach introduced in Sec. 4.1.3, reads:

$$\frac{dI(\mathbf{Q},\mathcal{F},\omega)}{d\Omega} = C(\Omega)\int_{-\infty}^{\infty} dt\, g(t) \sum_{I,r} P_{I,r}(\mathcal{F},\omega,t)$$
$$\left|\sum_{\mu} \sqrt{\mathcal{F}_\mu}\, e^{i\mathbf{Q}\cdot\mathbf{R}_\mu} \left[\sum_{X}\sum_{j=1}^{N_X} f_{X,I^\mu_{X,j}}(\mathbf{Q},\omega)\, e^{i\mathbf{Q}\cdot\mathbf{r}^\mu_{X,j}} + \sum_{l=1}^{N_e} e^{i\mathbf{Q}\cdot\mathbf{r}^\mu_{e,l}}\right]\right|^2 . \tag{4.1}$$

In this equation, **Q** is the momentum transfer, $\mathcal{F} = \{\mathcal{F}_\mu\}$ is the x-ray fluence distribution throughout the crystal, the index μ runs over all super-cells and ω is the photon energy. $C(\Omega)$ is a factor depending on the polarization of the x-ray pulse, and $g(t)$ represents the normalized temporal envelope. $f_{X,I^\mu_{X,j}}$ is the atomic form factor of the jth atom of species X in the μth super-cell, $I^\mu_{X,j}$ is the associated electronic configuration, $I = \{I^\mu_{X,j}\}$ denotes a global electronic configuration, $\mathbf{r}^\mu_{X,j}$ represents the position vector of the jth atom of species X in the μth super-cell, and $r = \{\mathbf{r}^\mu_{X,j}\}$ indicates the set of all atomic positions. N_X represents the total number of atoms for species X within a super-cell. $P_{I,r}$ represents the probability distribution of electronic configuration I and atomic positions r, and $\mathbf{R}_\mu$ represents the position of the μth super-cell. N_e represents the total number of free electrons in the μth super-cell, and $\mathbf{r}^\mu_{e,l}$ represents the position vector of the lth electron in the μth super-cell. The atomic form factor

$$f_{X,I^X_j}(\mathbf{Q},\omega) = f^0_{X,I^\mu_{X,j}}(\mathbf{Q}) + f'_{X,I^\mu_{X,j}}(\omega) + i f''_{X,I^\mu_{X,j}}(\omega) \tag{4.2}$$

includes the dispersion corrections $f'_{X,I^{\mu}_{X,j}}(\omega)$ and $if''_{X,I^{\mu}_{X,j}}(\omega)$. This dispersion correction can be neglected when the applied photon energy is high above the ionization edges, which is fulfilled in our study. Note that the summation over $\sqrt{\mathcal{F}_{\mu}}$ appears inside the modulus square in Eq. (4.1). The scattering amplitude from the $\mu\mathrm{th}$ super-cell is proportional to the x-ray field amplitude ($\propto \sqrt{\mathcal{F}_{\mu}}$) in that super-cell. A key assumption when performing the coherent sum in Eq. (4.1) is that the entire crystal is illuminated coherently, a condition that is fulfilled considering realistic XFEL beam parameters and crystal sizes.

XSINC: Scattering pattern simulation code

In order to construct the scattering pattern, Eq. (4.1) cannot be used directly as the P_I and r configuration space is too large. However, by calculating realizations of super-cell dynamics with XMDYN, a Monte-Carlo sampling of the distribution $P_{I,r}(\mathcal{F}, \omega, t)$ represented in Eq. (4.1) becomes feasible. To construct the time evolution of the crystal through global configurations and to calculate patterns, I used the following strategy, implemented in the code XSINC (x-ray scattering in nanocrystals).

Firstly, I discretized the fluence space and calculated many super-cell trajectories for each fluence value with XMDYN. XSINC selects randomly a trajectory for each super-cell within the crystal (a local realization), so that the corresponding fluence values are matching the best. These trajectories describe the local time evolution of the super-cells and together, they form a global realization of the crystal. Then, taking into account the spatial and temporal pulse profiles, XSINC calculates the scattering amplitudes and intensities for the global configuration at different times based on the corresponding snapshots. Finally, the incoherent sum of these patterns corresponds to a time integrated pattern measured in a single-shot experiment. In the calculation, I perform a dense sampling of the fluence space. As a consequence, two neighboring super-cells experience very similar fluence. Therefore, it is a good approximation to take into account the direct effect of the neighboring cells by applying periodic boundary conditions and this construction leads to a realistic global trajectory.

4.1.4 Results and Discussion

Simulation setup

In my investigations, I consider a diamond cube of a size of 1 μm. I investigate the cases of flattop and gaussian beam profiles (Fig. 4.2). Other parameters of the pulses are the same in both the cases: photon energy is 10 keV, total number of photons per x-ray pulse is $1{\times}10^{12}$, the temporal pulse envelope is gaussian with a duration of 10 fs FWHM, focus size is $100{\times}100\,\mathrm{nm}^2$ FWHM. The size of the diamond unit cell is $a = b = c =$ 3.57 Å containing 8 carbon atoms. The parameter choices listed in Table 4.1 yield converged results. In the scheme mentioned above, several parameters are convergence parameters of the method (Table 4.1). Results are considered converged when characteristic properties of the Bragg peaks, such as the width and the height of the intensity distribution in reciprocal space, converge during a monotonic increase (or decrease) of the parameter. As an example, Figures 4.1(a) and 4.1(b) illustrate the convergence of the time integrated peak intensity as a function of the number of local (super-cell) realizations per fluence point for the reflection (1 1 1) for the gaussian and the flattop spatial profile cases. We note that convergence implicitly depends on the total number of different realizations used to build a global realization. Therefore, in the gaussian case, where 350 different fluence points are used, convergence starts at a much smaller value.

Convergence Parameters	**Gaussian Case**	**Flattop Case**
Number of crystallographic unit cells in a super-cell	$5 \times 5 \times 5$	$5 \times 5 \times 5$
Number of fluence points	350	1
Number of local realizations (XMDYN trajectories) per fluence point	5	150
Number of assembled global realizations	10	10
Depth of the crystal in beam propagation direction	1 × Thickness of the super-cell lattice constant	1 × Thickness of the super-cell lattice constant
Number of snapshots	28	28

TABLE 4.1: Convergence parameters for calculating scattering intensity with XSINC and their values in the current study. This table is taken from Ref. [5]

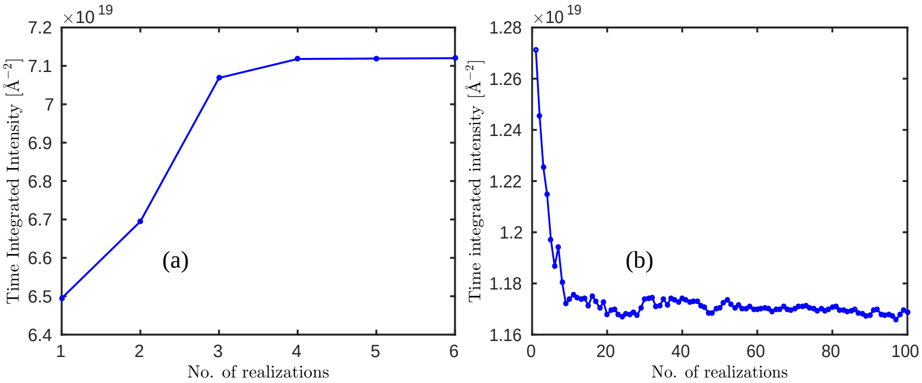

FIGURE 4.1: Convergence of time integrated peak intensity for the reflection (1 1 1) as a function of the number of realizations per fluence point: (a) for the gaussian and (b) for the flattop spatial pulse profile. For the gaussian case, 350 different fluence points are used to calculate the time integrated intensity. This figure is taken from Ref. [5]

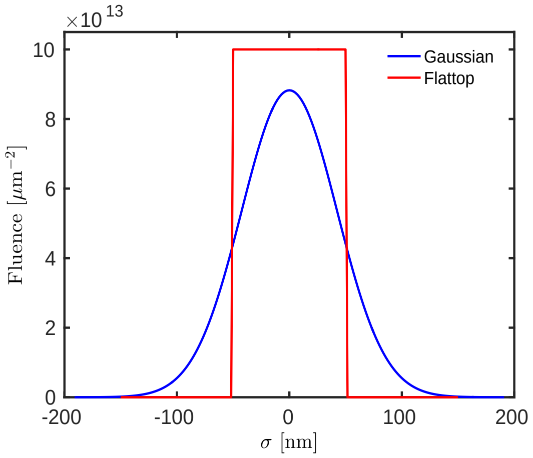

FIGURE 4.2: Radial fluence distributions in the current study: gaussian profile (spatially non-uniform case) and flattop profile (uniform within the irradiated part of the crystal). The focal size is 100 nm in both cases and the pulse energy is also considered to be same. This figure is taken from Ref. [5].

Radiation damage

The coherent scattering patterns depend on the presence of the atomic bound electrons as well as on the atomic positions. The XMDYN and XATOM simulations allow to analyze their change due to radiation damage for both diamond and isolated carbon atom cases. Radiation damage is initiated by atomic photoionization events. In case of isolated carbon atoms, Auger decays contribute approximately to the same extent to the overall ionization. At the maximum fluence in our study, $\sim 35\,\%$ of the atoms are photoionized (Fig. 4.3.a). Although the absorbed energy is 10 keV per photon, almost all of this energy is taken away from the atom by the high-energy photoelectron. The picture is different when the atom is embedded in a crystal environment (Fig. 4.3.c). The high-energy photoelectrons stay within the medium and distribute their energy by causing further ionization via secondary ionization events. As a consequence, neutral atoms disappear early in the pulse and by the end, even fully stripped carbon ions (C^{6+}) appear. Many electrons are promoted to (quasi-)free states within the sample. This also illustrates the importance

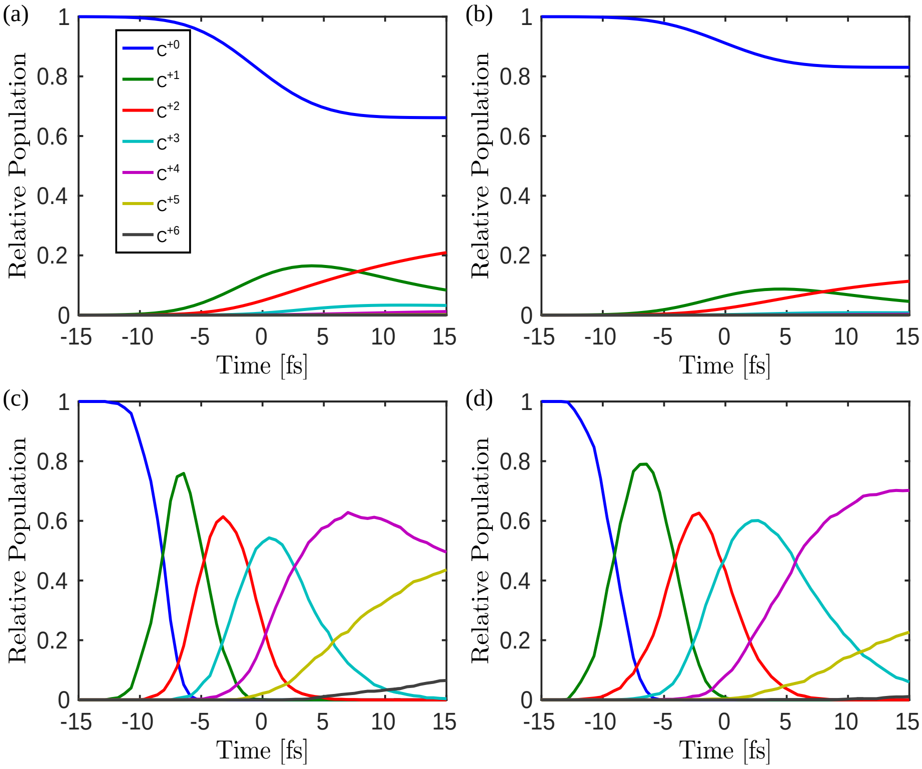

FIGURE 4.3: Ionization dynamics of carbon atoms at different fluences: time dependent charge state populations of isolated carbon atoms calculated with XATOM for (a) $\mathcal{F}_{\text{high}} = 1 \times 10^{14}\,\mu\text{m}^{-2}$ and (b) $\mathcal{F}_{\text{mid}} = 4.5 \times 10^{13}\,\mu\text{m}^{-2}$. Similarly, time dependent charge state populations of carbon atoms in diamond calculated with XMDYN for (c) $\mathcal{F}_{\text{high}}$ and (d) $\mathcal{F}_{\text{mid}}$. Secondary ionization events enhance the overall ionization in a dense environment. The x-ray pulse with 10 fs FWHM temporal profile is centered at $t = 0$ fs. This figure is taken from Ref. [5].

of secondary ionization processes in the progress of radiation damage in a dense environment [96, 97, 98]. In the center of the focus, the sample absorbs 3.5 keV energy per atom that heats up the plasma electrons besides the ionization. Despite the high charge states, recombination remains negligible during the pulse (number of events less than 1 % per atom in the simulation) due to the extreme conditions.

Figure 4.4 represents the mean displacement of the carbon atoms during the pulse. The average atomic displacement is much below the maximum achievable resolution, ~ 1.2Å at 10 keV, even at the highest fluence. This suggests that the patterns are affected predominantly due to the bound-electron loss through the modification of atomic scattering form factors. Despite the heavy ionization, atomic displacements remain negligible during the ultrashort pulse duration due to the highly symmetrical sample environment. We note here again that in my calculations, I neglected the chemical bonds. In low fluence regions, bonds may survive and stabilize the structure against the emerging Coulomb forces. As the observed displacements are far below the resolution even without any stabilization due to bonds, bondless modeling of the current scenario is applicable.

Effect of the PBC approach on the dynamics

While ionic motion is negligible during the pulse, fast photoelectrons can travel long distances. However, PBC confines all plasma electrons artificially within the supercell they have been created in. Neglecting particle transport may lead to error in (i) local plasma electron density and (ii) local energy density. Whenever a photoelectron is ejected, it leaves behind a positive charge located on an ion. If I consider Coulomb interaction only, a positive space charge would build up in a central cylinder because of photoelectron escape. Photoelectron trapping within the interaction volume would start early in the pulse, at an average ion charge as low as +0.005. An analogous phenomenon is discussed for finite samples in the literature [47]. However, photoelectrons cause secondary ionization as well, so an atomic bound electron is promoted to a low energy continuum state. If this slow electron is created in an outer region, it can efficiently contribute to the screening of the space charge the photoelectron left behind. Based on these arguments, one can conclude that (i) considering the interaction region to be neutral is a good approximation

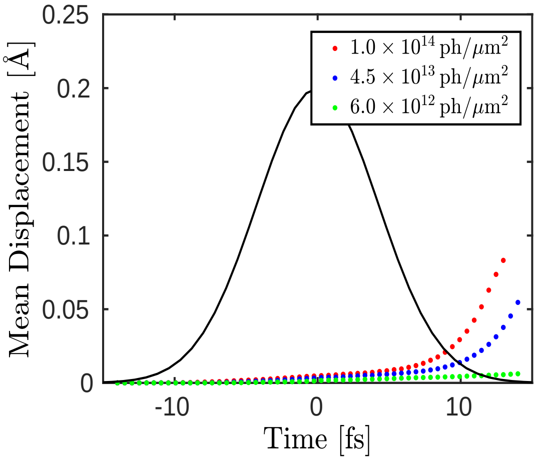

FIGURE 4.4: Mean displacement of the atoms for fluences $\mathcal{F}_{\text{high}} = 1{\times}10^{14}\ \mu m^{-2}$ (red dots), $\mathcal{F}_{\text{mid}} = 4.5{\times}10^{13}\ \mu m^{-2}$ (blue dots) and $\mathcal{F}_{\text{low}} = 6.0{\times}10^{12}\ \mu m^{-2}$ (green dots). The gaussian temporal pulse envelope is also depicted with the dashed black line. $\mathcal{F}_{\text{high}}$ is the fluence for the flattop profile, which is also the maximum fluence in the present study. $\mathcal{F}_{\text{mid}}$ and $\mathcal{F}_{\text{low}}$ are two values representing intermediate and low fluences taken from the gaussian profile case. The mean atomic displacement remains below the achievable resolution (~ 1.2Å) at 10keV for all the cases. This figure is taken from Ref. [5].

and (ii) in all regions, I overestimate the energy density by confining fast photoelectrons within a supercell. Similarly, as the Coulomb forces are the driving forces of the ionic motions, I may also overestimate the atomic/ionic displacements. In my study, eventually the effect on the scattering signal is relevant, as will be discussed in the next section.

Scattering with damage

In this section, I analyze the changes of the Bragg peak intensity profiles in reciprocal space due to the severe radiation damage. In Fig 4.5(a) and 4.5(b), snapshots of the 1D Bragg peak profiles in reciprocal space are depicted for the reflection $Q = (1\ 1\ 1)$ for Gaussian and flattop spatial beam profiles, respectively. Two apparent features can be seen, valid for other reflections as well.

1. The width of the Bragg peak does not change during the pulse. This is consistent with the expectation based on the negligible ion displacements – no visible Debye-Waller-like broadening occurs. However, the widths are different for the gaussian and flattop cases. The reason is the difference between the size of the illuminated parts of the crystal. In the flattop profile case, the focus size defines strictly the region exposed. On the other hand, a gaussian profile has no sharp edge and therefore illuminates a larger region, yielding a narrower Bragg peak and a larger effective crystal size.

2. Snapshots of the Bragg peak intensities behave differently for flattop and gaussian beams. The snapshots of the Bragg intensities depend not only on the scattering power of the sample, but also on the instantaneous x-ray intensity. However, as the instantaneous x-ray intensities are equal at the same time before and after the maximum of the pulse, a direct comparison of the corresponding snapshots of the Bragg profiles reflects exclusively the effect of different damage extents. In the gaussian profile case, these corresponding curves show small difference only, indicating that a significant contribution is coming from regions in the crystal suffering little damage (Fig. 4.5.a). In contrast, applying a flattop pulse profile, the scattering pattern is formed only from extensively ionized parts of the crystal. A consequence of the loss of atomic bound-electrons is the decrease of the atomic form factors yielding significant signal drop for longer times (Fig. 4.5.b). The above findings are reflected by the time integrated signals that correspond to the situation one would encounter in an experiment (1D cut:Fig. 4.5.c,d; 2D cut: Fig. 4.6). Note that for the gaussian spatial profile there is only a small decrease of the signal compared to the ideal (no damage) case.

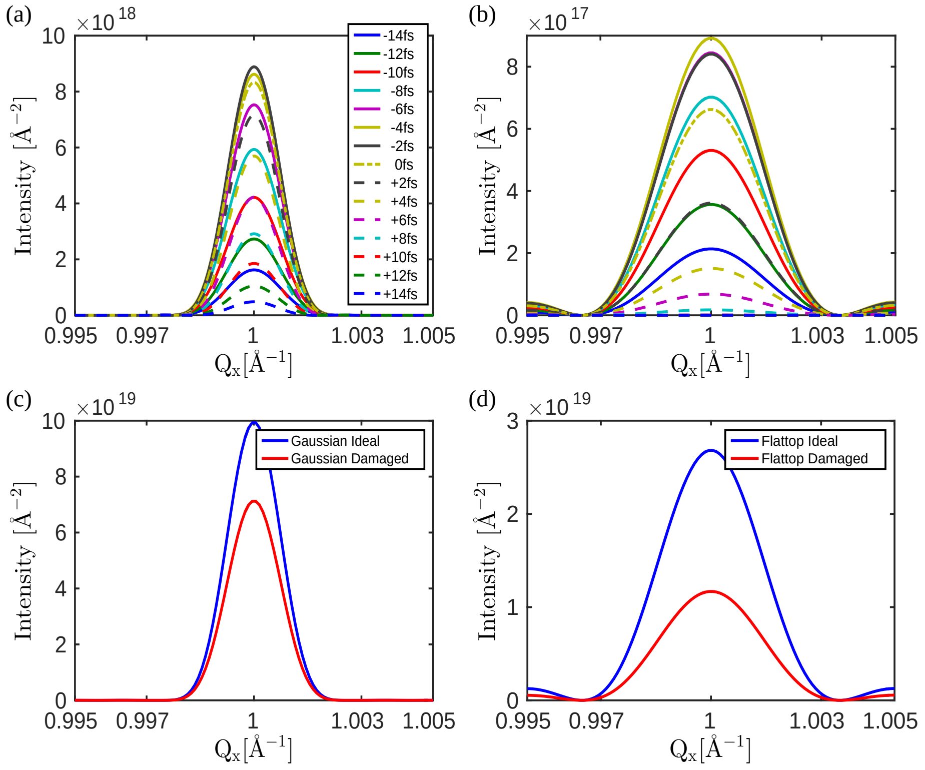

FIGURE 4.5: Snapshots of the scattering intensity for reflection (1 1 1) along the $Q_y = Q_z = 1\,\text{Å}^{-1}$ line in reciprocal space: (a) gaussian spatial beam profile, (b) flattop spatial beam profile. Solid and dashed lines with the same color correspond to the same instantaneous irradiating x-ray intensities. Note that the negative and the corresponding positive times are of equal intensity during the rise and fall of the pulse envelope. (c,d) Total time integrated scattering signal for gaussian and flattop spatial beam profiles, respectively. Note the different vertical axis scales. This figure is taken from Ref. [5].

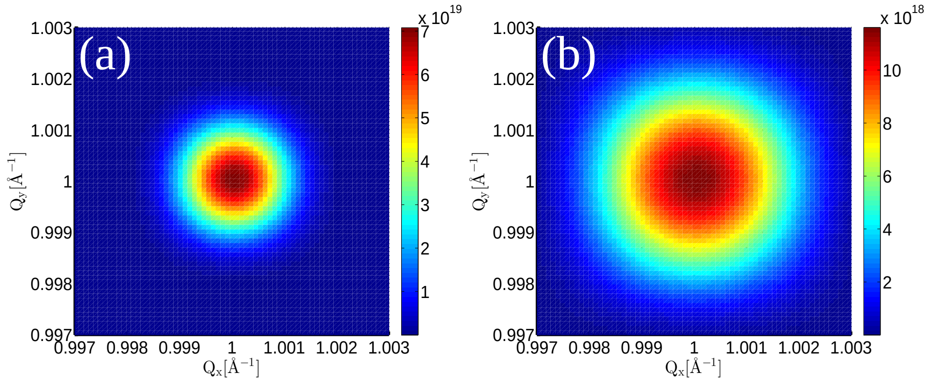

FIGURE 4.6: Contour plot for the Bragg spot of reflection (1 1 1) in the $Q_z = 1\,\text{Å}^{-1}$ plane in reciprocal space: (a) Gaussian beam profile; (b) flattop beam profile. This figure is taken from Ref. [5].

Effect of the PBC approach on the x-ray scattering patterns

Previously, I have discussed that the PBC approximation overestimates ionization and atomic displacements, and therefore radiation damage throughout the sample. It means that the method gives an upper bound to the effect of radiation damage on the scattering patterns. A trivial lower bound is the case without any radiation damage.

4.2 Towards the theoretical limitations of x-ray nanocrystallography at high intensity: the validity of the effective-form-factor description

4.2.1 Motivation

X-ray free-electron lasers (XFELs) broaden horizons in x-ray crystallography. Facilitated by the unprecedented high intensity and ultrashort duration of the XFEL pulses, they enable us to investigate structure and dynamics of macromolecules with nano-sized crystals. A limitation is the extent of radiation damage in the nanocrystal target. A large degree of ionization initiated by the incident high-intensity XFEL pulse alters the scattering properties of the atoms leading to perturbed measured patterns. I discuss the effective-form-factor approximation applied to capture this phenomenon and show the importance of temporal configurational fluctuations at high intensities, shaping these quantities besides the average electron loss. I analyze theoretically the applicability of the approach to targets consisting of several atomic species and also via realistic radiation damage simulations.

4.3 Theoretical methods

The scattering pattern of a crystal affected by severe radiation damage at high x-ray intensity is calculated by an *incoherent* summation over all possible electronic and nuclear configurations weighted by the corresponding probabilities of occurrence at a given time and then accumulated over the whole x-ray pulse. When a crystal is exposed to a high-intensity x-ray beam with fluence $\mathcal{F}$ and photon energy ω (I employ atomic units), the scattering intensity at the momentum transfer $\mathbf{Q}$, based on Eq. (4.1) is given by

$$\frac{dI(\mathbf{Q},\mathcal{F},\omega)}{d\Omega} = \mathcal{F}C(\Omega)\int_{-\infty}^{\infty} dt\, g(t) \sum_{\hat{I},\hat{R}} P_{\hat{I},\hat{R}}(\mathcal{F},\omega,t) \left| \sum_{X} \sum_{j=1}^{N_X} f_{X,I_j^X}(\mathbf{Q},\omega)\, e^{i\mathbf{Q}\cdot\mathbf{R}_j^X} \right|^2, \quad (4.3)$$

where X indicates the atomic species and j represents the atomic index of that species. $C(\Omega)$ represents a factor depending on the polarization of the x-ray pulse, while $g(t)$ is the normalized temporal envelope of the pulse. I assume a uniform fluence distribution within the irradiated part of the crystal [5]. $\hat{I} = \{I_j^X\}$ is the global electronic configuration of the crystal, which is given by specifying the electronic configuration I_j^X of all individual atoms, and $\hat{R} = \{\mathbf{R}_j^X\}$ is the global nuclear configuration of all atomic positions $\mathbf{R}_j^X$ in the nanocrystal. The atomic form factor differs for different atomic species X and different electronic configurations, so it is given by f_{X,I_j^X}. $P_{\hat{I},\hat{R}}$ is the time-dependent probability of $\hat{I}$ and $\hat{R}$, which also depends on $\mathcal{F}$ and ω. Note that it is critical to obtain the time evolution of $P_{\hat{I},\hat{R}}$ in order to evaluate the scattering intensity of equation (4.3).

In contrast, the scattering intensity for an undamaged sample is calculated simply by using a *coherent* sum (the dependence on $\mathbf{Q}$, $\mathcal{F}$, and ω is omitted for the sake of convenience),

$$\frac{dI}{d\Omega} = \mathcal{F}C(\Omega)\left|\sum_X f_X^0 \left(\sum_{j=1}^{N_X} e^{i\mathbf{Q}\cdot\mathbf{R}_j^X}\right)\right|^2, \tag{4.4}$$

where f_X^0 is the atomic form factor of the atomic species X in the neutral ground state. Here I consider nonresonant x-ray scattering only.

Our goal is to approximate the scattering intensity for XFEL-irradiated crystals by using a simple coherent form as in equation (4.4). The simplest solution can be obtained by replacing f_X^0 with the time-averaged atomic form factor,

$$\bar{f}_X = \int_{-\infty}^{\infty} dt\, g(t)\tilde{f}_X(t), \tag{4.5}$$

where $\tilde{f}_X(t) = \sum_{I_X} P_{I_X}(t)\, f_{I_X}$ is the time-dependent atomic form factor during the x-ray pulse and f_{I_X} is the atomic form factor of the I_Xth electronic configuration of the given atomic species X. $P_{I_X}(t)$ is the configurational population at a given time t, which was considered within the independent-atom model [35, 36]. The time-averaged atomic form factor $\bar{f}_X$ is typically interpreted by the effective charge for the given atomic species during the x-ray pulse. The effective charge (time-averaged electron loss) is enhanced as the intensity increases (see Fig. 4.8) because of ionization dynamics, thus reducing the time-averaged form factor.

On the other hand, it has been suggested that the time-averaged atomic form factor is not enough to describe the scattering intensity in the case of high-intensity x-ray fields [35, 36, 38]. Since the time-dependent atomic form factor varies dramatically during an intense x-ray pulse, one needs to take into account the temporal variance [36]. For a single atomic species, it is trivial to derive the following effective form factor from the generalized Karle-Hendrickson equation [35, 36]:

$$f_X^{\text{eff}} = \sqrt{\left|\bar{f}_X\right|^2 + V_X^{\text{time}}}, \tag{4.6}$$

where $V_X^{\text{time}} = \left(\int_{-\infty}^{\infty} dt\, g(t)|\tilde{f}_X(t)|^2\right) - \left|\int_{-\infty}^{\infty} dt\, g(t)\tilde{f}_X(t)\right|^2$. If the XFEL-irradiated crystal consists of more than one atomic species, one can show that the scattering intensity may be approximated by a coherent sum as in equation (4.4), with the effective atomic form factors defined in equation (4.6) (see Appendix for details). With this definition, one can clearly see the distinction between the effective form factor and that derived from the effective charge. Since $V_X^{\text{time}} > 0$, the time-averaged form factor $\bar{f}_X$ always underestimates the effective form factor f_X^{eff}. I will present a detailed numerical analysis for those form factors in the following section, based on realistic radiation damage simulations of nanocrystals irradiated by intense x-ray pulses. Note that the form of equation (4.6) is equivalent to that proposed in Ref. [99]: $f_X^{\text{eff}} = \sqrt{\int_{-\infty}^{\infty} dt\, g(t)\, \left|\tilde{f}_X(t)\right|^2}$.

4.4 Numerical analysis

4.4.1 Simulation methods

In order to perform a simulation of a nanocrystal exposed to an intense x-ray pulse, I subdivide the nanocrystal into supercells and simulate the ionization and nuclear dynamics for the supercells using XMDYN [1, 56, 57], applying periodic boundary conditions. To construct a scattering pattern from the nanocrystal, I employ the code XSINC [5].

In our investigation, for each Bragg reflection, XSINC analyzes the scattering intensity in equation (4.3) with $P_{\hat{I},\hat{R}}(t)$ obtained from realistic simulations of XMDYN, including both impact ionization and recombination, which are critical in a dense matter environment [5]. With $P_{I_X}(t)$ derived from $P_{\hat{I},\hat{R}}(t)$, the time-averaged atomic form factor $\bar{f}_X$ in equation (4.5) and the effective atomic form factor f_X^{eff} in equation (4.6) are calculated using XSINC.

4.4.2 Results

In my analysis, I consider a nanocrystal of the amino acid glycine. I use a photon energy of 10 keV and four different x-ray peak intensities: $I_1 = 1.5 \times 10^{18}\,\mathrm{W/cm^2}$, $I_2 = 1.5 \times 10^{19}\,\mathrm{W/cm^2}$, $I_3 = 1.5 \times 10^{20}\,\mathrm{W/cm^2}$ and $I_4 = 1.5 \times 10^{21}\,\mathrm{W/cm^2}$. The temporal pulse envelope is Gaussian with 10 fs full width at half maximum (FWHM) and I assume spatially uniform irradiation. In the simulation I choose a supercell consisting of 105 glycine molecules. For each peak intensity, 150 XMDYN trajectories are calculated. Figure 4.7 shows real-space snapshots of the atoms in a single supercell undergoing ionization as a function of time, for the intensities I_3 and I_4. It can be seen that the crystal structure is substantially modified by the end of the pulse for the I_4 case. Figure 4.8 shows the time evolution of the charge for different atomic species at different intensities. For the lowest intensity (I_1), almost all the species remain neutral (charges $< +0.3$) after irradiation, whereas for the highest intensity (I_4), carbon, nitrogen and oxygen are ionized up to charge states of +4.7, +5.2 and +6.0, respectively. To saturate single-photon absorption for light atoms (carbon, nitrogen and oxygen) at 10 keV, the intensity at 10 fs FWHM must be larger than 10^{21} W/cm^2. Therefore, x-ray multiphoton ionization does not play a significant role in the intensity regime under consideration, except for the highest intensity. The drastic changes in the charge states shown in the high-intensity cases in Fig. 4.8 are mainly due to electron impact ionization [5], resulting in severe radiation damage. The accuracy of the effective-form-factor approximation is verified by the crystallographic R-factor, which is widely used as a measure of the agreement between calculated patterns based on a crystallographic model and the experimental ones. In Fig. 4.9 I compare the goodness of two different approximations using

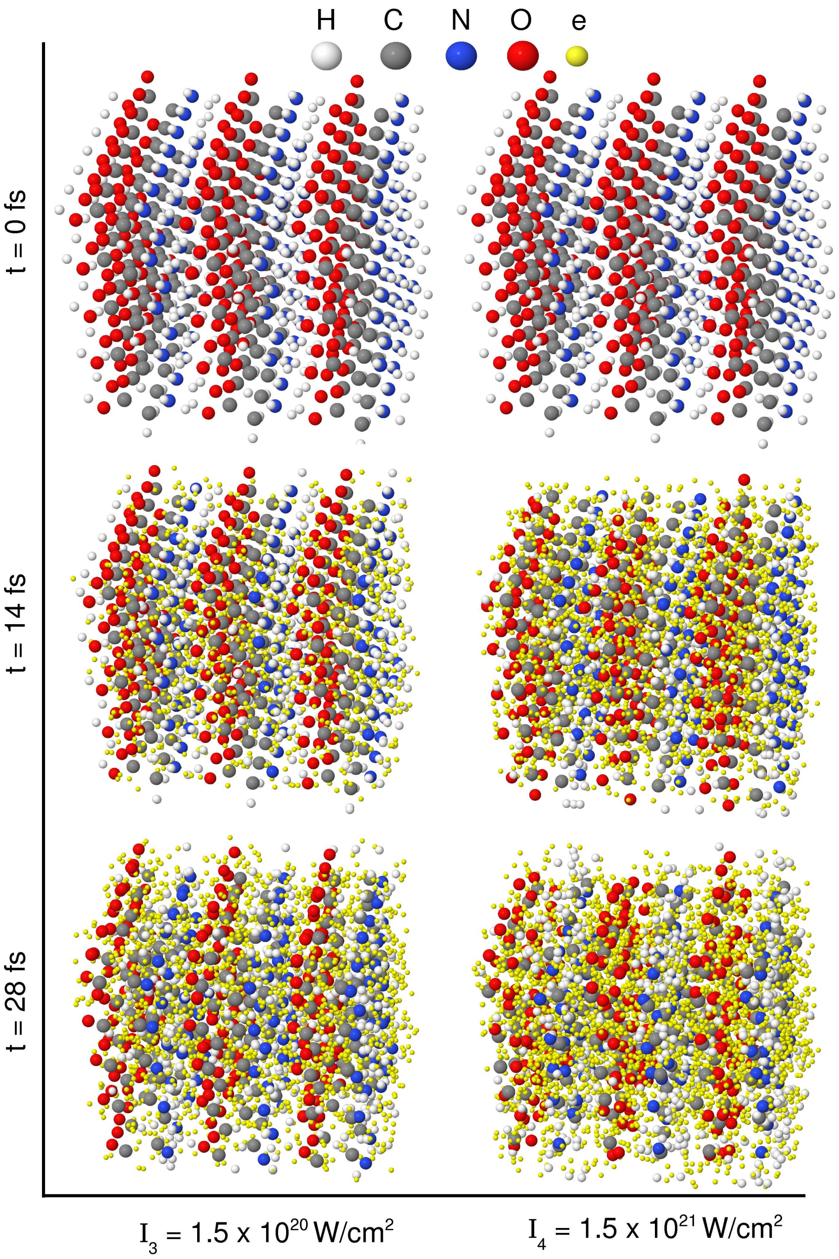
H
C
N
O
e
t = 0 fs
t = 14 fs
t = 28 fs
I$_3$ = 1.5 x 10^{20} W/cm^2
I$_4$ = 1.5 x 10^{21} W/cm^2

FIGURE 4.7: Real-space snapshots of ionization dynamics of a supercell comprising 105 molecules of glycine. The photon energy is 10 keV; the peak intensities are $I_3 = 1.5 \times 10^{20}\,\mathrm{W/cm^2}$ and $I_4 = 1.5 \times 10^{21}\,\mathrm{W/cm^2}$. The temporal pulse envelope is Gaussian with 10 fs full width at half maximum (FWHM). This figure is taken from Ref. [6]

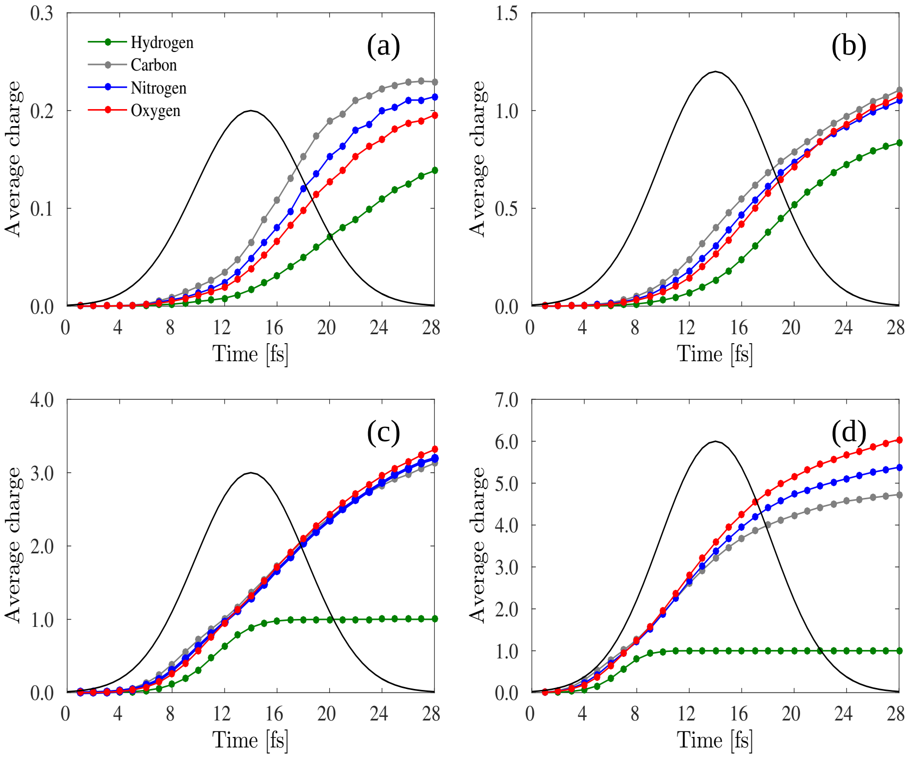

FIGURE 4.8: Average charge as a function of time at the intensity of (a) $I_1 = 1.5 \times 10^{18}\ \mathrm{W/cm^2}$, (b) $I_2 = 1.5 \times 10^{19}\ \mathrm{W/cm^2}$, (c) $I_3 = 1.5 \times 10^{20}\ \mathrm{W/cm^2}$ and (d) $I_4 = 1.5 \times 10^{21}\ \mathrm{W/cm^2}$. The red curve represents the temporal Gaussian envelope of 10 fs FWHM. This figure is taken from Ref. [6]

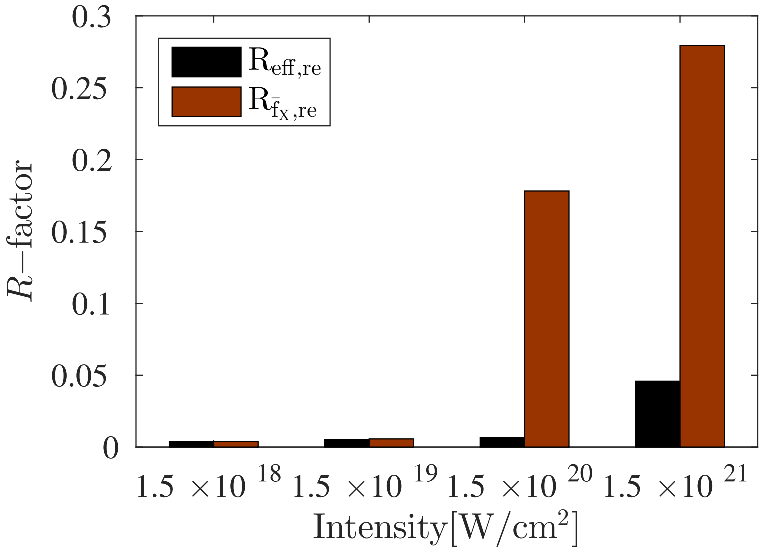

FIGURE 4.9: Crystallographic R-factor in two different cases as a function of intensity. The black bars represent $R_{\text{eff,re}}$, the brown bars represent $R_{\bar{\text{f}}_{\text{X}},\text{re}}$. This figure is taken from Ref. [6]

the R-factor at several intensities. $R_{\text{eff,re}}$ is defined by

$$R_{\text{eff,re}} = \frac{\sum_{\mathbf{Q}} \left| \sqrt{I_{\text{eff}}(\mathbf{Q})} - \sqrt{I_{\text{re}}(\mathbf{Q})} \right|}{\sum_{\mathbf{Q}} \sqrt{I_{\text{re}}(\mathbf{Q})}}, \tag{4.7}$$

where the *real* intensities $I_{\text{re}}(\mathbf{Q})$ are calculated from the incoherent sum, with full dynamics calculations, in equation (4.3) and $I_{\text{eff}}(\mathbf{Q})$ is calculated from the coherent sum in equation (4.4) by replacing f_X^0 with the *effective* form factors f_X^{eff} [equation (4.6)]. Similarly, $I_{\bar{\text{f}}_{\text{X}}}(\mathbf{Q})$ is obtained by replacing f_X^0 with $\bar{f}_X$. Then, $R_{\bar{\text{f}}_{\text{X}},\text{re}}$ is calculated from $I_{\bar{\text{f}}_{\text{X}}}(\mathbf{Q})$ and $I_{\text{re}}(\mathbf{Q})$. The R-factor value required for successful structural determination is suggested to be $R \leq 0.15$ as a rule of thumb [16]. The minimum possible value of R-factor is zero, indicating perfect agreement between the considered cases. It can be seen that for the highest intensity (I_4), $R_{\text{eff,re}}$ is still only about 0.05, which indicates good agreement between I_{eff} and I_{re}. Hence, the coherent sum with the effective atomic form factors used here can describe the radiation damage in a nanocrystal even for the highest intensity (I_4). On the other hand, $R_{\bar{\text{f}}_{\text{X}},\text{re}}$ increases

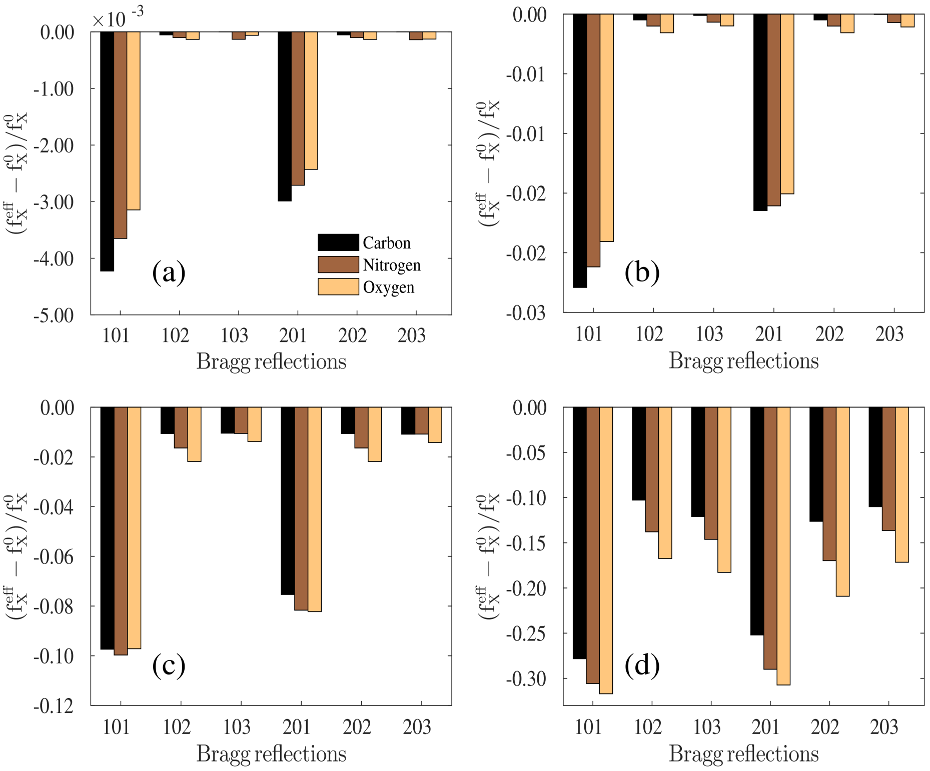

FIGURE 4.10: Relative differences of the effective form factor (f_X^{eff}) as compared to the ideal form factor (f_X^0) for different atomic species. The peak intensity for each panel is the same as used in Fig. 4.8. This figure is taken from Ref. [6]

much more rapidly as a function of the intensity, indicating that the time-averaged atomic form factor $\bar{f}_X$ is a poor choice when attempting to approximate the non-ideal pattern in terms of a coherent pattern; f_X^{eff} [equation (4.6)] provides a much better fit, particularly at the highest intensities considered here. To further explore the changes due to radiation damage dynamics using the effective form factors, I analyze the relative difference between the effective and ideal (undamaged) form factors, $\left(f_X^{\mathrm{eff}} - f_X^0\right)/f_X^0$, as shown in Fig. 4.10. The effective atomic form factors are always reduced because of the radiation damage, so all plots in Fig. 4.10 are negative. The relative differences are almost negligible at low intensities [see (a) and (b)], but not anymore at high intensities; the maximum difference is about 10% in

(c) and 30% in (d), respectively. Moreover, these relative differences are not constant for different Bragg reflections and different atomic species. For example, at the lowest intensity in (a), the effective form factors of carbon at the (1 0 1) and (2 0 1) reflections are more reduced than those of oxygen, even though the percentage is very small. At the highest intensity in (d), the f_X^{eff} of oxygen are more reduced than those of carbon, and the relative differences fluctuate between 10% and 30% for different Bragg reflections. Hence, the effective form factors cannot in general be obtained by multiplying the standard form factors f_X^0 by a single uniform scaling factor.

Chapter 5

Application: imaging of progressing radiation damage in real time

This chapter is based on an experiment that was performed at the LCLS [95]. It includes the complete methodology of the simulations that I have explained in the course of this thesis. The chapter focuses exclusively on my simulation work, i.e., without including any experimental results as the experimental data analysis is still in progress at the time of preparing this thesis.

The goal of the experiment was to image the evolution of the radiation damage using two-color time-delayed pulses. The first pulse initiates the dynamics, but the elastically scattered photons are filtered out. The second pulse has a slightly lower frequency, so that the elastically scattered photons can pass through the filter and can be detected, imprinting the progressive damage on the scattering pattern. I will start with the radiation damage simulations and will finally proceed towards the calculation of the scattering patterns.

5.1 Setup: sample and simulation conditions

In order to do the simulation of the damage of an irradiated complex system of 5-amino-2,4,6-triiodoisophthalic acid (I3C) in crystalline form consisting of heavy and light atomic species, I have used XMDYN, in junction with XATOM. It is not feasible to simulate the dynamics of a ∼micron-sized irradiated crystal when each atom is followed individually. Therefore, I used the following approach. I picked a few representative fluence values between zero and the maximum fluence (local fluence at the center of the Gaussian focus). I calculated the dynamics of the atoms and electrons within individual crystal unit cells subjected to these fluences applying PBC. I repeated the calculations with different random seeds several times in order to sample the stochastic dynamics for better statistics. For irradiation simulations, I considered pulse parameters used for the experiment recently performed at the LCLS free-electron laser [95]. The computational cell used in the simulations contained 8 molecules of I3C (184 atoms in total). The photon energy for both pump and probe pulses was 9.7 keV (I neglected the small difference in the photon energy of the two pulses) and the pulse duration was 10 fs (FWHM). Two different fluences were considered in the simulations – a high fluence of $\mathcal{F}_{\text{high}} = 1.0 \times 10^{13}\,\text{ph}/\mu\text{m}^2$ (estimated to be at the center of the focus), and a medium fluence of $\mathcal{F}_{\text{med}} = 5.0 \times 10^{12}\,\text{ph}/\mu\text{m}^2$. The beam focus is considered to be 150 nm. Different time delays were considered between 0 fs and 110 fs. But for the sake of convenience, only the results for 0 fs, 20 fs, 40 fs, 80 fs and 110 fs time delays are shown. For the analysis, 50 XMDYN trajectories are calculated for both the fluence cases.

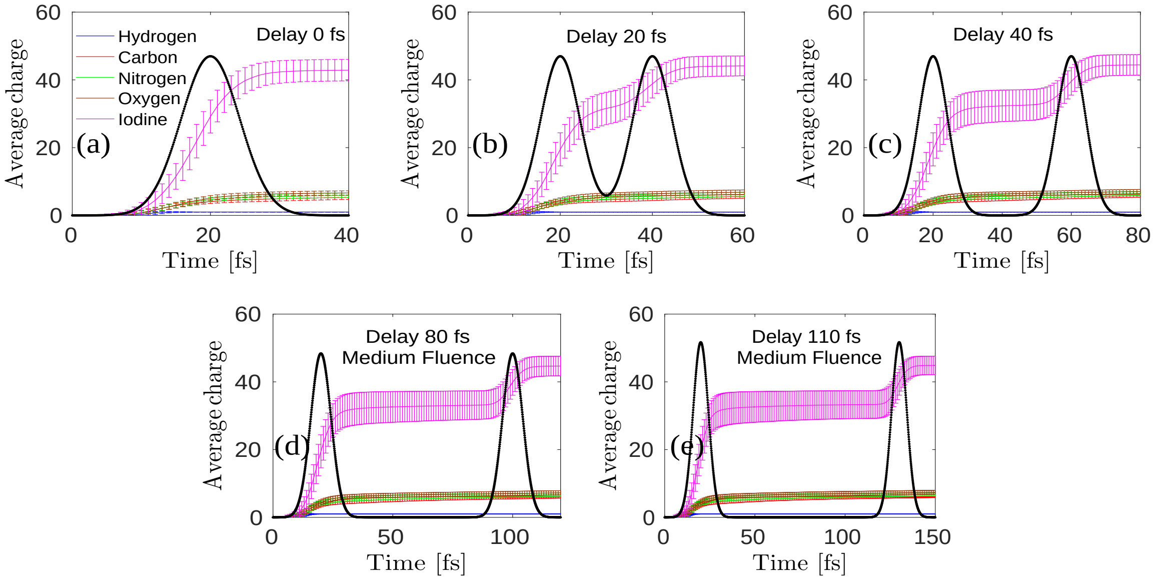

FIGURE 5.1: Average charge as a function of time, representing (a) 0 fs delay, where the two pulses are coincident, (b) 20 fs delay, (c) 40 fs delay, (d) 80 fs delay and (e) 110 fs delay. The black curve represents the temporal Gaussian envelope of 10 fs FWHM. The fluence considered is $\mathcal{F}_{\text{med}} = 5.0 \times 10^{12}\,\text{ph}/\mu\text{m}^2$; the average charge is calculated using 50 trajectories for each delay.

5.1.1 Results and Discussion on radiation damage

Figure 5.1 shows the time evolution of charges for $\mathcal{F}_{\text{med}}$. Extreme ionization of the system even during the pump pulse is observed for $\mathcal{F}_{\text{med}}$. Almost all the light atoms are fully ionized and the average charge state of iodine goes up to +34. The average charge state increases further to +41 during the probe pulse. The main ionization channel observed at $\mathcal{F}_{\text{med}}$ is photoionization and the subsequent Auger decay for iodine atoms. Impact ionization also played an important role in ionizing iodine and this is the predominant process to ionize the light atoms such as carbon, nitrogen and oxygen. For different time delays, the real time propagation is only considered until the probe pulse is over.

Figure 5.2 shows the time evolution of charges for $\mathcal{F}_{\text{high}}$. The average charge state goes up to +41 for iodine, which increases further to +47 during the probe

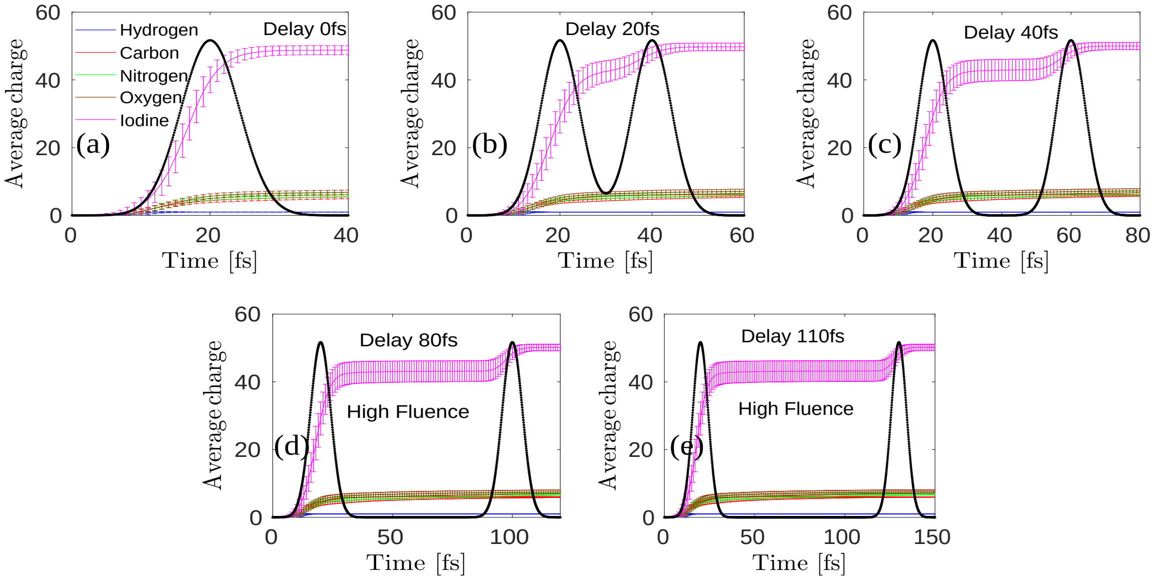

FIGURE 5.2: Average charge as a function of time, representing (a) 0 fs delay, where the two pulses are coincident, (b) 20 fs delay, (c) 40 fs delay, (d) 80 fs delay and (e) 110 fs delay. The black curve represents the temporal Gaussian envelope of 10 fs FWHM. The fluence considered is $\mathcal{F}_{\text{high}} = 1.0\times10^{13}\,\text{ph}/\mu\text{m}^2$; the average charge is calculated using 50 trajectories for each delay.

pulse. Impact ionization after photoionization and Auger decay play an important role in stripping off electrons from iodine atoms. Even at the end of the probe pulse, simulations show ionization due to impact ionization for iodine atoms. This shows that highly energetic photo-electrons still exist and can induce more damage at longer time scales. It may be noted that the system after the probe pulse is not yet thermalized.

Figure 5.3 represents the mean displacement as a function of time delay for $\mathcal{F}_{\text{med}}$. Hydrogen atoms are already displaced ~0.5 Å during the pump pulse. The mean displacement increases further to ~1.2 Å during the probe pulse. The heaviest atomic species, namely iodine, is displaced on average, ~0.25 Å. Other atoms like carbon, nitrogen and oxygen are displaced up to ~0.5 Å for the maximum delay case.

Figure 5.4 represents the mean displacement as a function of time delay for $\mathcal{F}_{\text{high}}$.

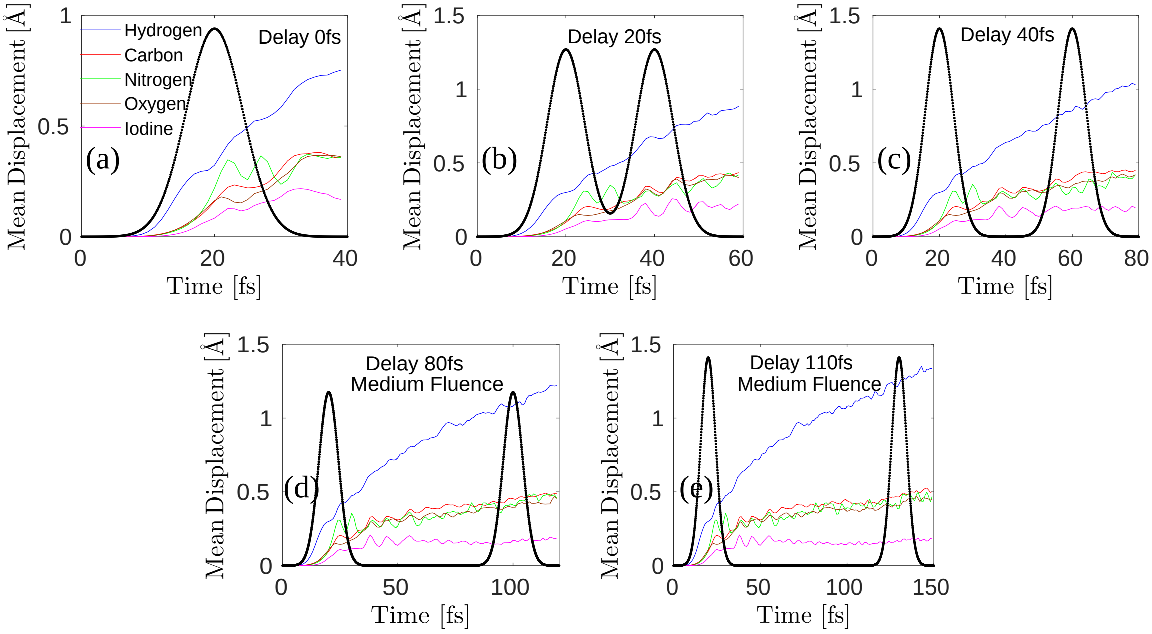

FIGURE 5.3: Mean displacement as a function of time, representing (a) 0 fs delay, where the two pulses are coincident, (b) 20 fs delay, (c) 40 fs delay (d) 80 fs delay and (e) 110 fs delay. The black curve represents the temporal Gaussian envelope of 10 fs FWHM. The fluence considered is $\mathcal{F}_{\text{med}} = 5.0 \times 10^{12}\,\text{ph}/\mu\text{m}^2$; the mean displacement is calculated using 50 trajectories for each delay.

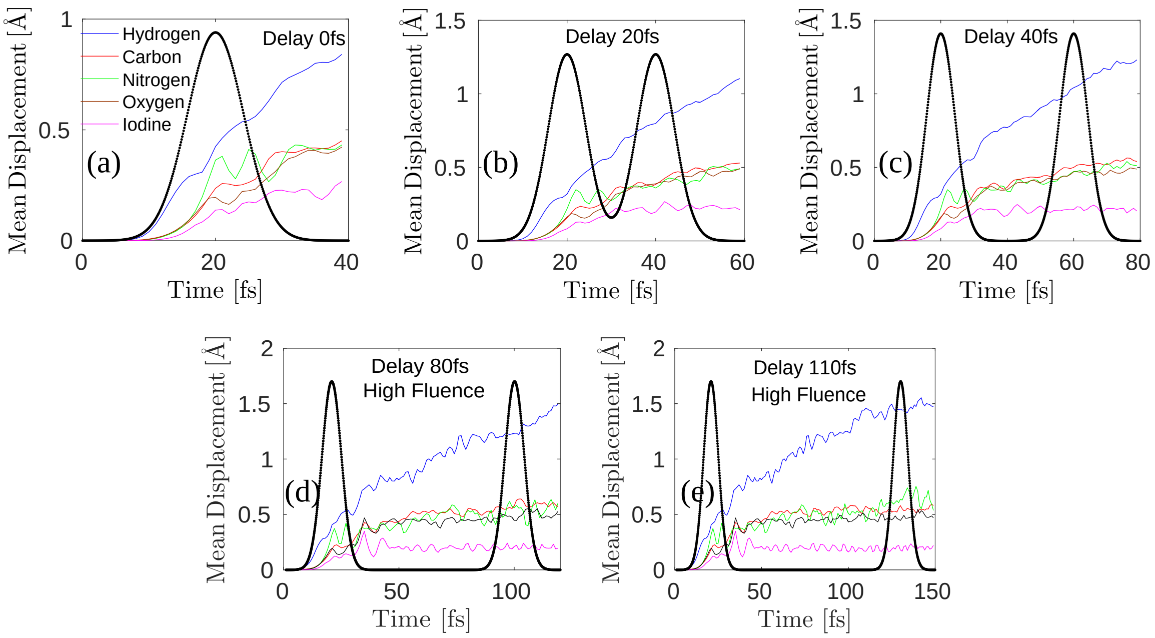

FIGURE 5.4: Mean displacement as a function of time, representing (a) 0 fs delay, where the two pulses are concident, (b) 20 fs delay, (c) 40 fs delay, (d) 80 fs delay and (e) 110 fs delay. The black curve represents the temporal Gaussian envelope of 10 fs FWHM. The fluence considered is $\mathcal{F}_{\text{high}} = 1.0\times10^{13}\,\text{ph}/\mu\text{m}^2$; the mean displacement is calculated using 50 trajectories for each delay case.

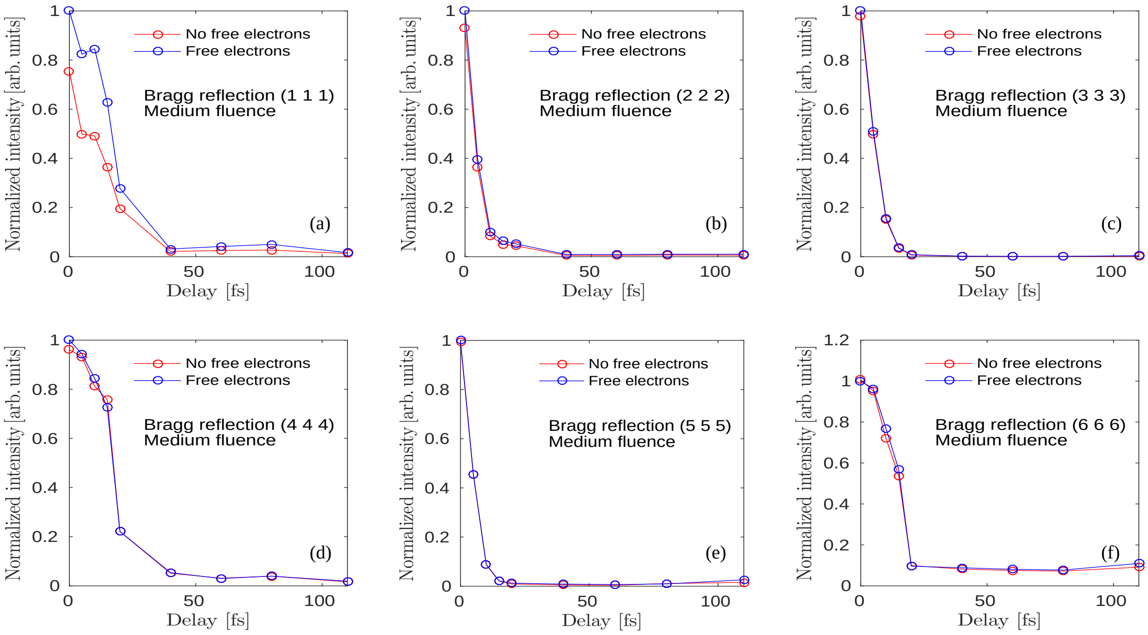

FIGURE 5.5: Time and volume integrated scattering intensity as a function of time delay, corresponding to Bragg reflections (a) (1 1 1), (b) (2 2 2), (c) (3 3 3), (d) (4 4 4), (e) (5 5 5) and (f) (6 6 6). The red curve represents the scattering intensity without the contribution of the free electrons, whereas the blue curve represents the scattering intensity from both bound and free electrons. The fluence considered is $\mathcal{F}_{\text{med}} = 5.0 \times 10^{12}$ ph/μm^2.

The trend is similar to that of $\mathcal{F}_{\text{med}}$ case. It can be seen that for 0 fs delay, carbon, nitrogen and oxygen atoms are already displaced up to ∼0.5Å. Iodine atoms are displaced by ∼0.25 Å on an average. Displacement for iodine atoms is not siginificant, which is basically due to the following reasons:

(1) the heavy nuclues of the iodine atoms,

(2) the charge screening, which restricts the motion of the iodine atoms.

5.1.2 Results and Discussion on scattering intensity and patterns

In order to calculate the scattering pattern, I used a fixed fluence scenario; i.e., I assumed a uniform spatial fluence distribution within the illuminated volume. I constructed a crystal with a diameter of the focal size by choosing randomly from the

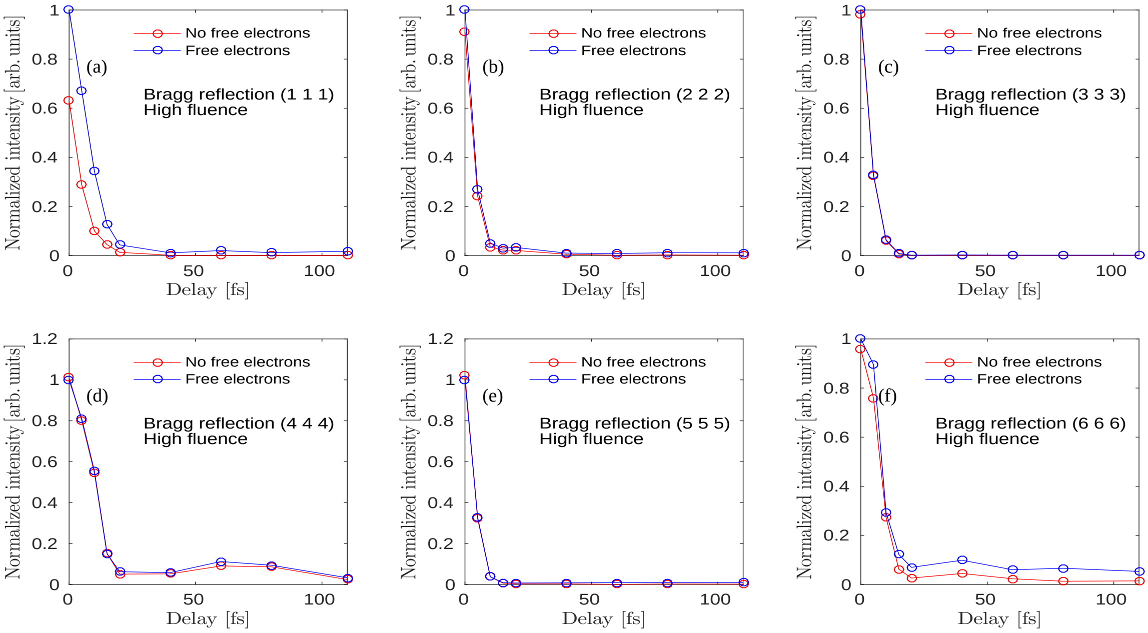

FIGURE 5.6: Time and volume integrated scattering intensity as a function of time delay, corresponding to Bragg reflections (a) (1 1 1), (b) (2 2 2), (c) (3 3 3), (d) (4 4 4), (e) (5 5 5) and (f) (6 6 6). The red curve represents the scattering intensity without the contribution of the free electrons, whereas the blue curve represents the scattering intensity from both bound and free electrons. The fluence considered is $\mathcal{F}_{\text{high}} = 1.0\times10^{13}\,\text{ph}/\mu\text{m}^2$.

calculated unit cell trajectories (driven by the same fluence) as its building blocks. I calculated the time integrated scattering signal for different reflections (**Q**-vectors in reciprocal space) based on the time evolution of the constructed crystal using XS-INC. The scattering signal has contribution from the bound electrons of the atoms as well as from the free electrons released during ionization events according to Eq. 4.1. The dispersion correction of the atomic form factors is also included.

Figure 5.5 represents the time and volume integrated scattering intensity as a function of time delay for different Bragg reflections. The fluence is set to $\mathcal{F}_{\mathrm{med}} = 5.0\times10^{12}\,\mathrm{ph}/\mu\mathrm{m}^2$. Considering only the scattering from the bound electrons only, the scattering intensity goes down significantly as a function of time delay for all the Bragg reflections. This is due to the decrease in the number of bound electrons due to photoionization, Auger decay and secondary ionization processes. When including the contribution from the free electrons, besides the enhancement of the background, an increase of the Bragg intensities can be observed for some reflections. This increase is due to the fact that strong correlation develops between the highly charged ions and the plasma electrons via the Coulomb forces. This correlation yields an increase of plasma electron density around the ions, enhancing the scattering power at the ionic positions. The density enhancement is a dynamical effect and depends on the number of localized electrons.

For $\mathcal{F}_{\mathrm{high}} = 1.0\times10^{13}\,\mathrm{ph}/\mu\mathrm{m}^2$, Fig. 5.6 represents the scattering intensity for different Bragg reflections as a function of time delay. The trends are very similar to that of the medium fluence case, but the effects are enhanced. One can see a more drastic decrease of intensity as a function of time and a stronger contribution of the free electrons to the Bragg reflections in Fig. 5.6. The reason is the higher depletion of the bound electrons and therefore stronger correlation effects between the ions with higher charge and the plasma electrons at higher density.

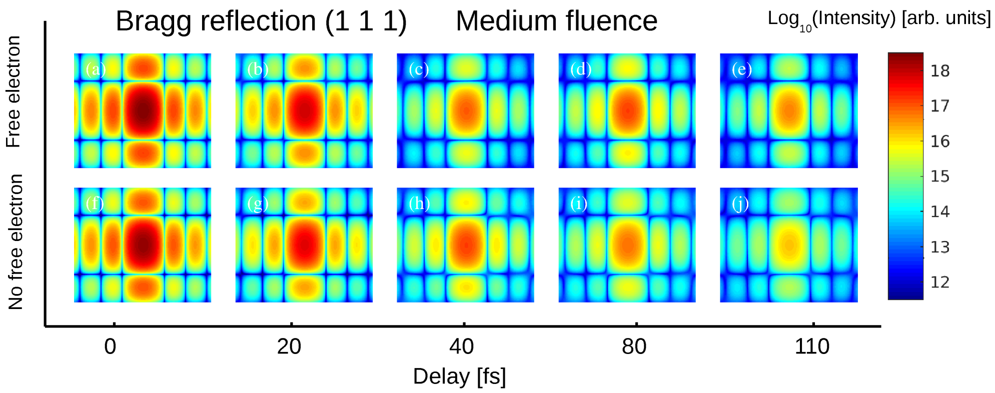

FIGURE 5.7: Contour plot for the Bragg reflection (1 1 1) in the $Q_z = 1\,\text{Å}^{-1}$ plane in reciprocal space for $\mathcal{F}_{\text{med}} = 5.0\times10^{12}\,\text{ph}/\mu\text{m}^2$. Figures (a-e) correspond to the scattering intensity including the free-electron term, whereas Figs. (f-j) illustrate the scattering intensity without the free-electron term.

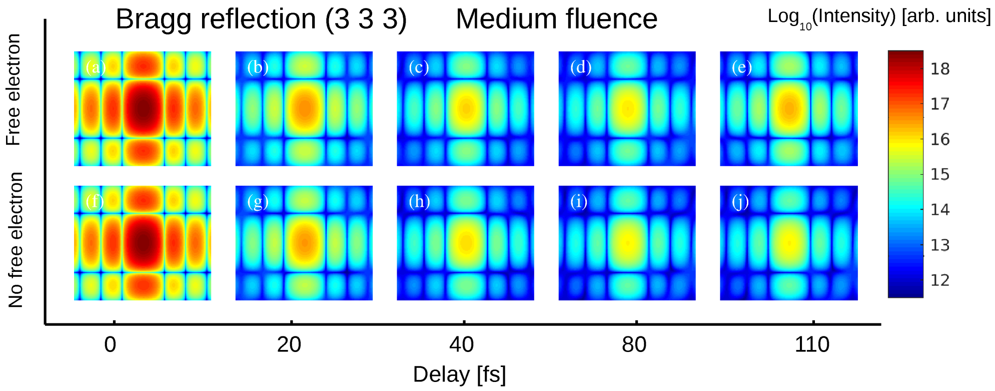

FIGURE 5.8: Contour plot for the Bragg reflection (3 3 3) in the $Q_z = 1\,\text{Å}^{-1}$ plane in reciprocal space for $\mathcal{F}_{\text{med}} = 5.0\times10^{12}\,\text{ph}/\mu\text{m}^2$. Figures (a-e) correspond to the scattering intensity including the free-electron term, whereas Figs. (f-j) illustrate the scattering intensity without the free-electron term.

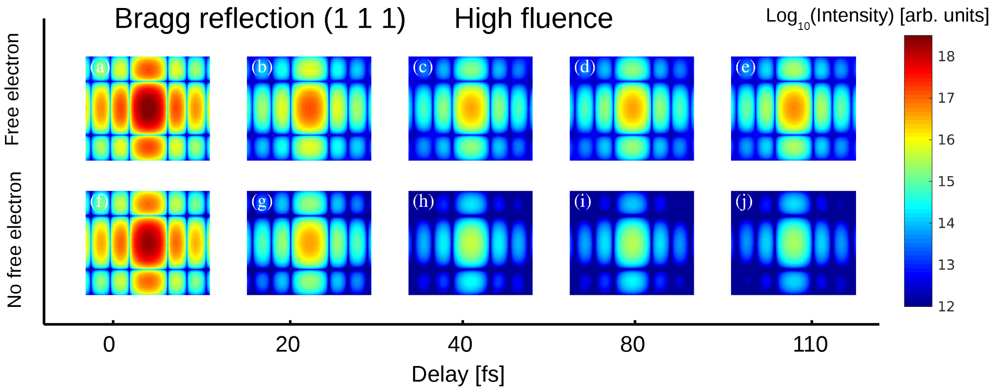

FIGURE 5.9: Contour plot for the Bragg reflection (1 1 1) in the $Q_z = 1\,\text{Å}^{-1}$ plane in reciprocal space for $\mathcal{F}_{\text{med}} = 1.0{\times}10^{13}\,\text{ph}/\mu\text{m}^2$. Figures (a-e) correspond to the scattering intensity including the free-electron term, whereas Figs. (f-j) illustrate the scattering intensity without the free-electron term.

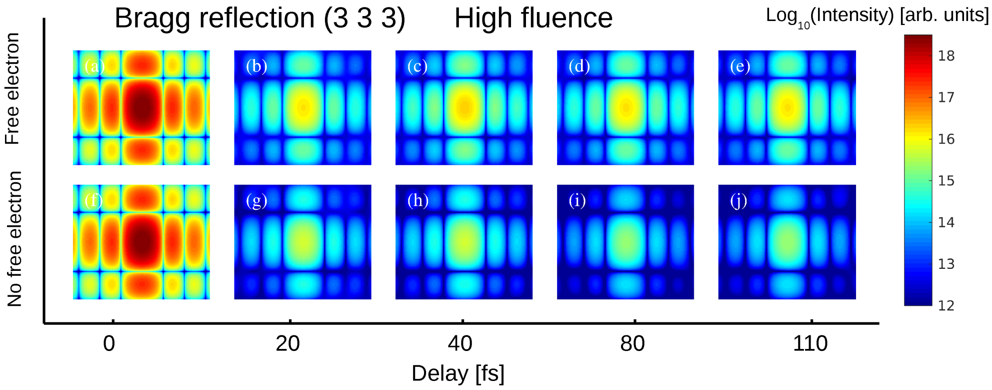

FIGURE 5.10: Contour plot for the Bragg reflection (3 3 3) in the $Q_z = 1\,\text{Å}^{-1}$ plane in reciprocal space for $\mathcal{F}_{\text{med}} = 1.0{\times}10^{13}\,\text{ph}/\mu\text{m}^2$. Figures (a-e) correspond to the scattering intensity including the free-electron term, whereas Figs. (f-j) illustrate the scattering intensity without the free-electron term.

The scattering signal increases due to the contribution of the free electrons. But it is not clear from the volume and time integrated signals whether this contribution is from the background or the Bragg peaks are actually enhanced. Figures 5.7 and 5.8 show contour plots of Bragg peaks (1 1 1) and (3 3 3) as a function of time delay for the medium fluence case, visualizing the scattered intensity distribution around the Bragg peak in reciprocal space rather than its volume integrated value.

It can be seen that for both low **Q** and high **Q**-values, the scattering intensity as a function of time delay decreases. But when including the free-electron term, the background as well as the peak intensity increases, compared to the contribution from the bound electrons only. Similarly, for the high fluence case, Figs. 5.9 and 5.10 represent the contour plots of time integrated scattering intensity. As a function of time delay, it can be seen that the scattering signal from bound electrons only almost disappears, whereas the Bragg peak is still visible when the free electron contribution is taken into account. These findings demonstrate the importance of the free- (or plasma-) electron contribution in the theoretical analysis of the scattering patterns.

Chapter 6

Conclusions

My research contributes to the field of high energy density plasma physics as well as the new emerging field of nanocrystallography, which also motivated this research. The thesis focuses on theoretical investigations of high intensity x-ray related scientific topics: (i) plasma formation and progression of radiation damage within micron sized crystals and bulk systems of organic molecules and carbon model systems due to an intense x-ray pulse and (ii) scattering pattern formation during irradiation. My work includes methodological and code developments (XSINC and periodic boundary condition extension to XMDYN) as well as applications of the simulation tools.

In *Chapter* 3, I have investigated the thermalization dynamics of x-ray-heated bulk carbon systems using the simulation tool XMDYN and compared its predictions to two other conceptually different simulation methods – the average-atom model and the Boltzmann continuum approach. Analyzing thermalization times, temperature and ionic charge state distributions within irradiated carbon systems, we found reasonable agreement between the model predictions. Such comparisons are important validation steps of the XMDYN approach that allows one to follow inhomogeneous non-equilibrium systems of ions of any species (e.g., heavy elements) with arbitrary electronic configuration.

In *Chapter* 4, I presented a methodology for the simulation of x-ray scattering patterns from serial femtosecond crystallography experiments with a high-intensity x-ray beam. My approach includes the simulation of radiation damage within the sample with the codes XMDYN and XATOM as well as the calculation of the patterns using the code XSINC. According to this approach, the time evolution (the radiation damage process) is calculated within sub-units of the crystal independently using periodic boundary conditions. Then, a nanocrystal is assembled from the sub-units for the calculation of the time integrated patterns. As a demonstration of the method, I investigated the spatial pulse profile effects on the Bragg peaks for a diamond nanocrystal. I found that if a gaussian profile is used (assuming realistic XFEL parameters, such as tight focus and ultrashort pulse duration), the time integrated signal intensity is reduced only by a small amount compared to the damage-free case. For a flattop profile (at the same pulse energy), the decrease is much more significant. The intensity reduction is primarily due to the change of the form factors caused by ionizations. In both cases, the width of the Bragg peak was connected to the size of the illuminated region in the crystal but was not affected by the damage. As our approach overestimates the radiation damage in the interaction region, it gives an upper bound to the effect of the radiation damage on the patterns.

Moreover, I have discussed the generalization of the effective-form-factor approximation applied to describe scattering patterns from XFEL-irradiated samples consisting of multiple atomic species. I have shown that these quantities are mainly shaped by the average electron loss caused by stochastic ionization events and dynamical configurational fluctuations. I have demonstrated via realistic numerical simulations that the role of the latter contribution becomes more prominent with increasing x-ray intensity. Still, up to intensities relevant for XFELs, the effective-form-factor description is acceptable, also implying that conventional structure-reconstruction algorithms dealing with purely coherent scattering signals can be expected to work in this intensity regime as well.

In $Chapter$ 5, motivated by an experiment, I have investigated the progression of the radiation damage within an I3C nanocrystal by applying a realistic pump-probe scheme in the calculations. Under the experimental conditions, the ionization damage increases fast in time, driven by the photoionization of iodine atoms; therefore, the scattering signal strength decreases. The scattering signal is lost after 20 fs in the simulations. The reason is the depletion of the bound electrons as well as the motion of the nuclei. Furthermore, I have investigated the effect of free-electron contribution to the scattering signal. A significant increase of the Bragg intensities can be observed when including this contribution due to the ion-free electron correlations; a dynamical electron density enhancement can be observed around the highly charged heavy ions. This result demonstrates that theoretical predictions without the free-electron contribution underestimate the scattering signal.

Appendix A

Effective-form-factors derivation

In a similar fashion as in Ref. [38], the effective atomic form factor is defined by the square root of the scattering intensity given by only one atomic species X after averaging over time and configurations:

$$f_X^{\text{eff}} = \sqrt{\frac{\mathcal{F}C(\Omega)\int_{-\infty}^{\infty} dt\, g(t) \sum_{\hat{I},\hat{R}} P_{\hat{I},\hat{R}}(\mathcal{F},\omega,t) \left| \sum_{j=1}^{N_X} f_{X,I_j^X}\, e^{i\mathbf{Q}\cdot\mathbf{R}_j^X} \right|^2}{\mathcal{F}C(\Omega)\int_{-\infty}^{\infty} dt\, g(t) \sum_{\hat{I},\hat{R}} P_{\hat{I},\hat{R}}(\mathcal{F},\omega,t) \left| \sum_{j=1}^{N_X} e^{i\mathbf{Q}\cdot\mathbf{R}_j^X} \right|^2}}. \tag{A.1}$$

I assume that the nanocrystal is exposed to a homogeneous fluence distribution [5]. Assuming that no nuclear motions are involved during the short pulse duration and radiation damage dynamics of individual atoms happen individually, the global population is given by the product of the individual atomic populations with the corresponding electronic configuration,

$$P_{\hat{I},\hat{R}}(\mathcal{F},\omega,t) = \prod_X \prod_{j=1}^{N_X} P_{I_j^X}(\mathcal{F},\omega,t). \tag{A.2}$$

Also I assume the dynamical profiles of individual atomic populations to be similar to each other for a given atomic species, $P_{I_j^X}(\mathcal{F},\omega,t) \approx P_{I_X}(\mathcal{F},\omega,t)$. Then the effective atomic form factor goes over into

$$f_X^{\text{eff}} = \sqrt{\int_{-\infty}^{\infty} dt\, g(t) \left|\tilde{f}_X(t)\right|^2 + \left[N_X \left(\sum_{I_X} \bar{P}_{I_X} \left|f_{I_X}\right|^2 - \int_{-\infty}^{\infty} dt\, g(t) \left|\tilde{f}_X(t)\right|^2\right) \Big/ \left|\sum_{j=1}^{N_X} e^{i\mathbf{Q}\cdot\mathbf{R}_j^X}\right|^2\right]}$$
$$\approx \sqrt{\int_{-\infty}^{\infty} dt\, g(t) \left|\tilde{f}_X(t)\right|^2} = \sqrt{\left|\bar{f}_X\right|^2 + V_X^{\text{time}}}, \tag{A.3}$$

where $\bar{P}_{I_X} = \int_{-\infty}^{\infty} dt\, g(t) P_{I_X}(t)$ (the dependence of $\mathcal{F}$, $\mathbf{Q}$ and ω is omitted). A similar analysis was performed in Ref. [35]. The term within the brackets in equation (A.3) diminishes when N_X becomes large, because at Bragg peaks $\left|\sum_{j=1}^{N_X} e^{i\mathbf{Q}\cdot\mathbf{R}_j^X}\right|^2 \propto (N_X)^2$. It is worthwhile to note that this definition of the effective atomic form factor is directly connected to the MAD coefficient $\tilde{a}_X$ in Ref. [35]: $f_X^{\text{eff}} = f_X^0\sqrt{\tilde{a}_X}$.

Next, I demonstrate how the scattering intensity may be approximated by a coherent sum using the effective form factors. I start from equation (2) in Appendix A in Ref. [37]. For simplicity, I consider only two atomic species, A and B (an extension to many atomic species is straightforward):

$$\frac{dI}{d\Omega} = \mathcal{F}C(\Omega) \int_{-\infty}^{\infty} dt\, g(t) \sum_{\hat{I}} P_{\hat{I}}(\mathcal{F}, \omega, t) \left|\sum_{j=1}^{N_A} f_{A,I_j^A}(\mathbf{Q}, \omega) e^{i\mathbf{Q}\cdot\mathbf{R}_j^A} + \sum_{k=1}^{N_B} f_{B,I_k^B}(\mathbf{Q}, \omega) e^{i\mathbf{Q}\cdot\mathbf{R}_k^B}\right|^2. \tag{A.4}$$

Following the expressions in Ref. [37], the scattering intensity is written as the extended Karle–Hendrickson equation,

$$\frac{dI}{d\Omega} = \mathcal{F}C(\Omega)\Big[\left|F_A^0\right|^2 \tilde{a}_A + N_A \left|f_A^0\right|^2 (a_A - \tilde{a}_A) + \left|F_B^0\right|^2 \tilde{a}_B + N_B \left|f_B^0\right|^2 (a_B - \tilde{a}_B)$$
$$+ \left|F_A^0\right| \left|F_B^0\right| B_{AB} \cos \Delta\phi_{AB}^0 + \left|F_A^0\right| \left|F_B^0\right| C_{AB} \sin \Delta\phi_{AB}^0\Big], \tag{A.5}$$

where the molecular form factor is defined by

$$F_X^0 = f_X^0 \sum_{j=1}^{N_X} e^{i\mathbf{Q}\cdot\mathbf{R}_j^X} = \left|F_X^0\right| e^{i\phi_X^0}, \tag{A.6}$$

and the phase difference is $\Delta\phi_{AB}^0 = \phi_A^0 - \phi_B^0$. Note that the dependence on $\mathbf{Q}$ and ω is omitted for simplicity. The atom-specific MAD coefficients are given by

$$a_X = \frac{1}{\left(f_X^0\right)^2} \sum_{I_X} \bar{P}_{I_X} \left|f_{I_X}\right|^2, \tag{A.7}$$

$$\tilde{a}_X = \frac{1}{\left(f_X^0\right)^2} \int_{-\infty}^{\infty} dt\, g(t) \left|\tilde{f}_X(t)\right|^2, \tag{A.8}$$

and the biatom-specific MAD coefficients are defined by

$$B_{AB} = \frac{2}{f_A^0 f_B^0} \int_{-\infty}^{\infty} dt\, g(t) \left[\Re(\tilde{f}_A(t))\Re(\tilde{f}_B(t)) + \Im(\tilde{f}_A(t))\Im(\tilde{f}_B(t))\right], \tag{A.9}$$

$$C_{AB} = \frac{2}{f_A^0 f_B^0} \int_{-\infty}^{\infty} dt\, g(t) \left[\Re(\tilde{f}_A(t))\Im(\tilde{f}_B(t)) - \Im(\tilde{f}_A(t))\Re(\tilde{f}_B(t))\right]. \tag{A.10}$$

After plugging the effective form factor f_X^{eff} into equation (A.5), the scattering intensity is recast as

$$\begin{aligned} \frac{dI}{d\Omega} = \mathcal{F}C(\Omega)\Bigg[& \left|\frac{F_A^0}{f_A^0} f_A^{\text{eff}} + \frac{F_B^0}{f_B^0} f_B^{\text{eff}}\right|^2 + N_A \bar{V}_A^{\text{config}} + N_B \bar{V}_B^{\text{config}} \\ & + \left|F_A^0\right| \left|F_B^0\right| \left(B_{AB} - \frac{2 f_A^{\text{eff}} f_B^{\text{eff}}}{f_A^0 f_B^0}\right) \cos\Delta\phi_{AB}^0 + \left|F_A^0\right| \left|F_B^0\right| C_{AB} \sin\Delta\phi_{AB}^0 \Bigg], \end{aligned} \tag{A.11}$$

where $\bar{V}_X^{\text{config}} = \left(f_X^0\right)^2 \left(a_X - \tilde{a}_X\right)$ [36]. Under Bragg conditions, the terms with $\bar{V}_X^{\text{config}}$ are smaller than others as N_X becomes larger. When anomalous scattering contributions are small enough (for example, light atoms at hard x-rays), the term with C_{AB}

may be neglected. In addition, let us assume that time profiles of the dynamical behavior of different atomic species are proportional to $h(t)$, such that $\tilde{f}_A(t) = f_A^0 h(t)$ and $\tilde{f}_B(t) = f_B^0 h(t)$. The factor $\left(B_{AB} - \{2 f_A^{\text{eff}} f_B^{\text{eff}}\}/\{f_A^0 f_B^0\}\right)$ then becomes

$$\begin{aligned} B_{AB} - \frac{2 f_A^{\text{eff}} f_B^{\text{eff}}}{f_A^0 f_B^0} &= \frac{2}{f_A^0 f_B^0} \int_{-\infty}^{\infty} dt\, g(t)\, \tilde{f}_A(t) \tilde{f}_B(t) - \frac{2}{f_A^0 f_B^0} \sqrt{\int_{-\infty}^{\infty} dt\, g(t) \left|\tilde{f}_A(t)\right|^2} \sqrt{\int_{-\infty}^{\infty} dt\, g(t) \left|\tilde{f}_B(t)\right|^2} \\ &= 2 \int_{-\infty}^{\infty} dt\, g(t)\ (h(t))^2 - 2 \sqrt{\left(\int_{-\infty}^{\infty} dt\, g(t)\ |h(t)|^2\right)^2} = 0. \end{aligned} \tag{A.12}$$

Consequently, if I assume small anomalous scattering signals and similar dynamical behavior for different atomic species, and neglect small $N_X \bar{V}_X^{\text{config}}$ terms, then the scattering intensity may be expressed as the conventional coherent sum,

$$\begin{aligned} \frac{dI}{d\Omega} &= \mathcal{F}C(\Omega) \left| \frac{F_A^0}{f_A^0} f_A^{\text{eff}} + \frac{F_B^0}{f_B^0} f_B^{\text{eff}} \right|^2 \\ &= \mathcal{F}C(\Omega) \left| f_A^{\text{eff}} \left(\sum_{j=1}^{N_A} e^{i\mathbf{Q}\cdot\mathbf{R}_j^A} \right) + f_B^{\text{eff}} \left(\sum_{j=1}^{N_B} e^{i\mathbf{Q}\cdot\mathbf{R}_j^B} \right) \right|^2 . \end{aligned} \tag{A.13}$$

Bibliography

[1] Z. Jurek, S.-K. Son, B. Ziaja, R. Santra, *J. Appl. Cryst.* **49**, 1048 (2016).

[2] M. M. Abdullah, Anurag, Z. Jurek, S.-K. Son, R. Santra, *Phys. Rev. E* **96**, 023205 (2017).

[3] Y.-K. Kim, M. E. Rudd, *Phys. Rev. A* **50**, 3954 (1994).

[4] B. Ziaja, *et al.*, *Phys. Rev. E* **93**, 053210 (2016).

[5] M. M. Abdullah, *et al.*, *Struct. Dyn.* **3**, 054101 (2016).

[6] M. M. Abdullah, S.-K. Son, Z. Jurek, R. Santra, *Manuscript submitted* (2018).

[7] H. N. Chapman, *et al.*, *Nature* **470**, 73 (2011).

[8] A. Barty, *et al.*, *Nature Photon.* **6**, 35 (2012).

[9] S. Boutet, *et al.*, *Science* **20**, 362 (2012).

[10] L. Redecke, *et al.*, *Science* **339**, 227 (2013).

[11] N. Berrah, P. H. Bucksbaum, *Sci. Am.* **310**, 64 (2014).

[12] P. Emma, *et al.*, *Nature Photon.* **4**, 641 (2010).

[13] R. Neutze, *Phil. Trans. R. Soc. B* **369**, 20130318 (2014).

[14] H. N. Chapman, C. Caleman, N. Timneanu, *Phil. Trans. R. Soc. B* **369**, 20130313 (2014).

[15] H. N. Chapman, *Synchrotron Radiation News* **28**, 6 (2015).

[16] R. Neutze, R. Wouts, D. van der Spoel., E. Weckert, J. Hajdu, *Nature* **406**, 752 (2000).

[17] M. J. Bogan, *et al.*, *Nano Letters* **8(1)**, 310 (2008).

[18] S. P. Hau-Riege, R. A. London, G. Huldt, H. N. Chapman, *Phys. Rev. E* **71**, 061919 (2005).

[19] S. P. Hau-Riege, R. A. London, *et al.*, *Phys. Rev. Lett.* **98**, 198302 (2007).

[20] H. N. Chapman, K. A. Nugent, *Nature Photon.* **4**, 833 (2010).

[21] A. Aquila, A. Barty, *et al.*, *Structural Dynamics* **2**, 041701 (2015).

[22] Z. Jurek, G. Oszlányi, G. Faigel, *Eur. Phys. Lett.* **65**, 491 (2004).

[23] A. Barty, *et al.*, *Nature Photon.* **2**, 415 (2008).

[24] E. F. Garman, *Acta Crystallogr. D* **66**, 339 (2010).

[25] S. Boutet, G. J. Williams, *New J. Phys.* **12**, 035024 (2010).

[26] C. Caleman, *et al.*, *ACS Nano* **5**, 139 (2011).

[27] H. M. Quiney, K. A. Nugent, *Nature Phys.* **7**, 142 (2011).

[28] S.-K. Son, L. Young, R. Santra, *Phys. Rev. A* **83**, 033402 (2011).

[29] J. R. Fienup, *Appl. Opt.* **21**, 2758 (1982).

[30] S. Marchesini, *et al.*, *Phys. Rev. B* **68**, 140101 (2003).

[31] S. P. Hau-Riege, R. A. London, A. Szoke, *Phys. Rev. E* **69**, 051906 (2004).

[32] T. A. White, *et al.*, *Journal of Applied Crystallography* **45**, 335 (2012).

[33] J. Guss, *et al.*, *Science* **241**, 806 (1988).

[34] W. Hendrickson, *Science* **254**, 51 (1991).

[35] S.-K. Son, H. N. Chapman, R. Santra, *Phys. Rev. Lett.* **107**, 218102 (2011).

[36] S.-K. Son, H. N. Chapman, R. Santra, *J. Phys. B* **46**, 164015 (2013).

[37] L. Galli, *et al.*, *J. Synchrotron Radiat.* **22**, 249 (2015).

[38] L. Galli, *et al.*, *IUCrJ* **2**, 627 (2015).

[39] R. Fung, V. Shneerson, D. K. Saldin, A. Ourmazd, *Nature Phys.* **45**, 64 (2009).

[40] V. Elser, *IEEE Trans. Inf. Theor.* **55**, 4715 (2009).

[41] H. A. Scott, *J. Quant. Spectrosc. Radiat. Transfer* **71**, 689 (2001).

[42] M. Bergh, N. Timneanu, D. van der Spoel, *Phys. Rev. E* **70** (2004).

[43] Z. Jurek, G. Faigel, M. Tegze, *Eur. Phys. J. D* **29**, 217 (2004).

[44] B. Ziaja, A. de Castro, E. Weckert, T. Möller, *Eur. Phys. J. D* **40**, 465 (2006).

[45] C. Gnodtke, U. Saalmann, J. M. Rost, *Phys. Rev. A* **79**, 041201(R) (2009).

[46] C. Caleman, *et al.*, *J. Mod. Opt.* **58**, 1486 (2011).

[47] S. P. Hau-Riege, *Phys. Rev. Lett.* **108**, 238101 (2012).

[48] L. Fang, *et al.*, *Phys. Rev. Lett.* **109**, 263001 (2012).

[49] B. Rudek, *et al.*, *Nature Photon.* **6**, 858 (2012).

[50] H. Fukuzawa, *et al.*, *Phys. Rev. Lett.* **110**, 173005 (2013).

[51] A. Bar-Shalom, J. Oreg, W. H. Goldstein, D. Shvarts, A. Zigler, *Phys. Rev. A* **40**, 3183 (1989).

[52] O. Peyrusse, *J. Phys. B* **33**, 4303 (2000).

[53] J. Bauche, C. Bauche-Arnoult, M. Klapisch, *Atomic properties in hot plasmas* (Springer Verlag, Berlin, 2015).

[54] H.-K. Chung, M. H. Chen, W. L. Morgan, Y. Ralchenko, R. W. Lee, *High Energy Density Phys.* **1**, 3 (2005).

[55] H.-K. Chung, M. H. Chen, W. L. Morgan, Y. Ralchenko, *J. Quant. Spectrosc. Radiat. Transfer* **38**, 131 (1987).

[56] B. Murphy, Z. Jurek, *et al.*, *Nat. Commun.* **5**, 4281 (2014).

[57] T. Tachibana, Z. Jurek, *et al.*, *Sci. Rep.* **5**, 10977 (2015).

[58] S.-K. Son, R. Thiele, Z. Jurek, B. Ziaja, R. Santra, *Phys. Rev. X* **4**, 031004 (2014).

[59] B. F. Rozsnyai, *Phys. Rev. A* **5**, 1137 (1972).

[60] D. A. Liberman, *Phys. Rev. B* **20**, 4981 (1979).

[61] F. Perrot, *Phys. Rev. A* **25**, 489 (1982).

[62] O. Peyrusse, *J. Quant. Spectrosc. Radiat. Transfer* **99**, 469 (2006).

[63] A. Bar-Shalom, J. Oreg, M. Klapisch, *J. Quant. Spectrosc. Radiat. Transfer* **99**, 35 (2005).

[64] M. M. Abdullah, Z. Jurek, S.-K. Son, R. Santra, *J. Phys. Conf. Ser.* **635**, 102008 (2015).

[65] S.-K. Son, R. Santra, *Phys. Rev. A* **85**, 063415 (2012).

[66] J. M. Slowik, S.-K. Son, G. Dixit, Z. Jurek, R. Santra, *New Journal of Physics* **16**, 073042 (2014).

[67] G. Doumy, *et al.*, *Phys. Rev. Lett.* **106**, 083002 (2011).

[68] R. Santra, *J. Phys. B* **42**, 023001 (2009).

[69] J. C. Slater, *Phys. Rev.* **81**, 385 (1951).

[70] F. Herman, S. Skillman, *Atomic Structure Calculations* (Prentice-Hall, Englewood Cliffs, NJ, 1963).

[71] R. Latter, *Phys. Rev.* **99**, 510 (1955).

[72] G. H. Yao, S. I. Chu, *Chem. Phys. Lett.* **204**, 381 (1993).

[73] X. M. Tong, S. I. Chu, *Chem. Phys.* **217**, 119 (1997).

[74] J. W. Cooper, *Phys. Rev.* **128**, 681 (1962).

[75] S. T. Manson, J. W. Cooper, *Phys. Rev.* **165**, 126 (1968).

[76] F. Herman, S. Skillman, *Atomic Structure Calculations* (Prentice-Hall, Englewood Cliffs, NJ, 1963).

[77] E. Anderson, *et al.*, *LAPACK Users' Guide, 3rd ed.* (Society for Industrial and Applied Mathematics, Philadelphia, PA, 1999).

[78] S. P. Hau-Riege, *Phys. Rev. A* **76**, 042511 (2007).

[79] T. Koopmans, *Physica* **1**, 104 (1934).

[80] C. P. Bhalla, N. O. Folland, M. A. Hein, *Phys. Rev. A* **8**, 649 (1973).

[81] D. L. Walters, C. P. Bhalla, *Phys. Rev. A* **3**, 1919 (1971).

[82] D. Walters, C. Bhalla, *Atomic Data and Nuclear Data Tables* **3**, 301 (1971).

[83] R. N. Zare, *Angular momentum: Understanding Spatial Aspects in Chemistry and Physics* (Wiley Interscience, New York, NY, 1988).

[84] J.-P. Hansen, L. Verlet, *Phys. Rev.* **184**, 151 (1969).

[85] S. Bernard, G. L. Chiarotti, S. Scandolo, E. Tosatti, *Phys. Rev. Lett.* **81**, 2092 (1998).

[86] I. Georgescu, U. Saalmann, J. M. Rost, *Phys. Rev. A* **76** (2007).

[87] J. Kolfa, J. W. Perram, *Molecular Simulation* **9:5**, 351 (1992).

[88] M. Belhadj, H. Alper, R. Levy, *Chem. Phys. Lett.* **179**, 13 (1991).

[89] N. Metropolis, *et al.*, *J. Chem. Phys.* **21**, 1087 (1953).

[90] S. W. de Leeuw, J. W. Perram, E. R. Smith, *Proceedings of the Royal Society of London A: Mathematical, Physical and Engineering Sciences* **373**, 27 (1980).

[91] J. W. Perram, H. G. Peterson, S. W. de Leeuw, *Mol. Phys.* **65**, 875 (1988).

[92] M. A. Lennon, *et al.*, *J. Phys. Chem. Ref. Data* **17**, 1285 (1988).

[93] V. Saxena, B. Ziaja, *Phys. Plasmas* **23**, 012710 (2016).

[94] T. Beck, T. Gruene, G. M. Sheldrick, *Acta Cryst. D* **66**, 374 (2010).

[95] J. C. H. Spence, A. K. Richard, H. N. Chapman, D. Oberthuer, *Private Communication* .

[96] S. M. Vinko, *et al.*, *Nat. Commun.* **6**, 6397 (2015).

[97] S. M. Vinko, *et al.*, *Nature* **482**, 59 (2012).

[98] B. Ziaja, R. A. London, J. Hajdu, *J. Appl. Phys.* **97**, 064905 (2005).

[99] V. Y. Lunin, *et al.*, *Acta Crystallographica Section D* **71**, 293 (2015).